JOURNAL OF GEOPHYSICAL RESEARCH: SOLID EARTH, VOL. 118, 6025–6048, doi:10.1002/2013JB010408, 2013

Lithospheric deformation induced by loading of the Hawaiian Islands and its implications for mantle rheology

Shijie Zhong[1] and A. B. Watts[2]

Received 6 June 2013; revised 19 October 2013; accepted 28 October 2013; published 22 November 2013.

[1] The long-term rheological properties of the lithosphere are fundamental for understanding both surface tectonics and mantle dynamics on Earth. In this study, we have developed 3-D finite element models for computing the load-induced surface deformation and stress for lithosphere and mantle with realistic nonlinear viscoelastic rheology including the frictional sliding, low-temperature plasticity, and high-temperature creep. We have determined the lithospheric deformation and stress due to volcano loading in the Hawaiian Islands region for the last few million years. By comparing model predictions with seismic observations of the depth to the top of oceanic crust and depth dependence of seismicity in the Hawaiian Islands region, we have sought to constrain lithospheric rheology. Our calculations show that the load-induced surface deformation is controlled by low-temperature plasticity and frictional sliding but is insensitive to high-temperature creep. Lithospheric strength predicted from laboratory-derived low-temperature plasticity needs to be reduced significantly, and a frictional coefficient μ_f ranging from 0.1 to 0.7 is required in order to account for the observations. However, $\mu_f = 0.1$ weakens the shallow part of the lithosphere so much that it causes the minima in strain rate and stress to occur at too large depths to be consistent with the observed depth distribution of seismicity. Our results therefore suggest a value for μ_f between 0.25 and 0.7. Finally, the maximum stress that accumulates in the deformed lithosphere beneath the Hawaiian Islands is about 100–200 MPa for models that match the observations, and this stress may be viewed as the largest lithospheric stress on Earth.

Citation: Zhong, S. J., and A. B. Watts (2013), Lithospheric deformation induced by loading of the Hawaiian Islands and its implications for mantle rheology, *J. Geophys. Res. Solid Earth*, *118*, 6025–6048, doi:10.1002/2013JB010408.

1. Introduction

[2] An understanding of lithospheric rheology is fundamental to many branches of geodynamics including lithospheric dynamics, plate tectonics, mantle convection, and neotectonics. Two complementary approaches have been employed to study the rheology, and they are laboratory experiments on rock/crystal samples and modeling field-based observations. The focus to date has been the rheology of the mantle at sublithospheric conditions (i.e., at relatively high temperatures of >1100°C), including laboratory deformation experiments for olivine [e.g., *Hirth and Kohlstedt*, 2003; *Karato and Wu*, 1993; *Karato*, 2008] and field-based studies such as postseismic deformation [e.g., *Freed et al.*, 2010], glacial isostatic adjustment [e.g., *Peltier*, 1976; *Mitrovica and Forte*, 1997; *Paulson et al.*, 2007], and dynamic topography and geoid [e.g., *Hager and Richards*, 1989; *King*, 1995]. These studies have provided important constraints on the rheology of the sublithospheric mantle that help understand not only fundamental geodynamic processes such as long-wavelength mantle convection and supercontinent cycles [e.g., *Zhong et al.*, 2007a; *Höink et al.*, 2012] but also societally important questions including glacial ice loss and sea level rise for the present-day Earth [e.g., *Milne et al.*, 2009; *A et al.*, 2013].

[3] However, mantle rheology at lithospheric conditions (i.e., temperature <1100°C) is not as well understood [e.g., *Mei et al.*, 2010]. Laboratory studies suggest that rock deformation at lithospheric conditions operates at three different and highly nonlinear regimes: brittle or frictional sliding, semi-brittle, and plastic flow (Figure 1) [e.g., *Kohlstedt et al.*, 1995; *Mei et al.*, 2010]. Brittle and frictional sliding dominates lithospheric deformation at relatively shallow depths and low temperatures where lithospheric strength (i.e., yield stress) is controlled by Byerlee's law (Figure 1). At large depths and high temperatures, mantle deformation is controlled by two different mechanisms of plastic flow. For temperatures between ~400°C and ~800°C, mantle deformation is controlled by glide of dislocations with lattice resistance or the Peirels stress (i.e., low-temperature plasticity). For temperatures higher than ~800°C, the deformation is controlled by diffusion and dislocation creep (Figure 1). The semi-brittle regime is transitional between frictional sliding

---

[1] Department of Physics, University of Colorado, Boulder, Colorado, USA.

[2] Department of Earth Sciences, University of Oxford, Oxford, UK.

Corresponding author: S. Zhong, Department of Physics, University of Colorado at Boulder, Boulder, CO 80309–0390, USA. (szhong@colorado.edu)

©2013. American Geophysical Union. All Rights Reserved.
2169-9313/13/10.1002/2013JB010408

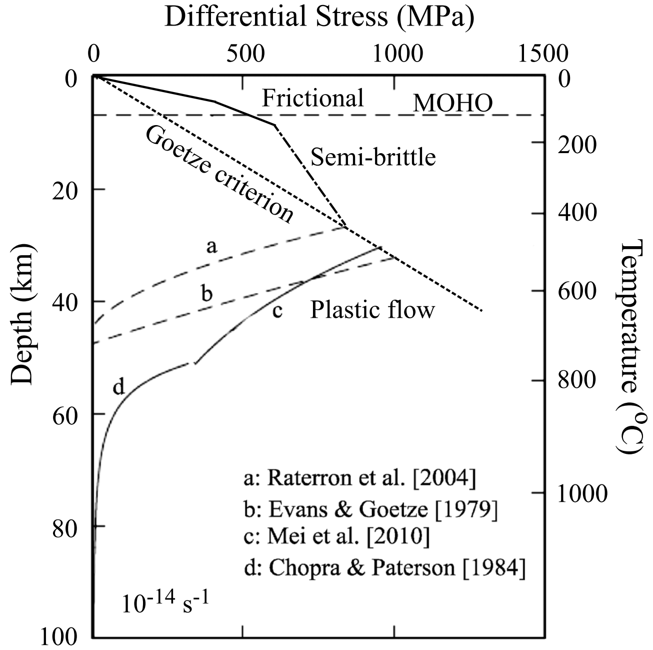

Figure 1. A schematic diagram (modified from *Mei et al.* [2010] and also see *Kohlstedt and Mackwell* [2009]) for lithospheric strength versus depth and temperature and for three lithospheric deformation regimes: frictional sliding, semi-brittle, and plastic flow. The plastic flow regime consists of two subregimes of the low-temperature plasticity and high-temperature creep. Curves a, b, and c represent three different published flow laws for the low-temperature plasticity, while curve d is for a high-temperature creep flow law. The frictional sliding limits the lithospheric strength for depth down to ~10 km before transitioning to the semi-brittle regime. The brittle-plastic transition (BPT) occurs where the low-temperature plasticity becomes dominant over the semi-brittle deformation (i.e., where the low-temperature plasticity flow law intercepts the Goetze criterion) [*Kohlstedt and Mackwell*, 2009].

and plastic flow (i.e., low-temperature plasticity) with multiple deformation mechanisms, and lithospheric strength is not well defined for this regime [*Kohlstedt and Mackwell*, 2009]. The multiple deformation regimes and their nonlinearity greatly limit the efficacy of laboratory and field-based in situ studies of lithospheric rheology.

[4] An important aspect of the rheology of the lithosphere is the yield strength. Yield strength envelope considerations (Figure 1) suggest that the upper lithosphere in the brittle and semi-brittle regimes has a strength greater than 500 MPa [e.g., *Kohlstedt and Mackwell*, 2009]. Such a high lithospheric strength appears to be consistent with field-based observations of stresses in the vicinity of oceanic islands and seamounts from flexural loading calculations [e.g., *Kanamori*, 1980; *Watts*, 2001]. However, lithospheric stresses and strength appear heterogeneous with much smaller stresses (i.e., tens of MPa) inferred for plate boundaries and regions of active faulting from thermal, seismic, and tectonic considerations [*Kanamori*, 1980; *Lachenbruch and Sass*, 1988]. The reduced lithospheric stress and strength in these tectonic settings may be associated with the dynamics of the faulting process, elevated pore pressure (hydration and serpentinization) [e.g., *Ruepke et al.*, 2009; *Byerlee*, 1978; *Kohlstedt et al.*, 1995], or slow healing of preexisting faults [e.g., *Gurnis et al.*, 2000].

[5] Plate tectonics is unique to Earth and has important controls on the dynamic evolution of our planet [e.g., *Bercovici*, 2003; *Davaille and Jaupart*, 1994]. However, it remains an open question as to how plate tectonics emerges from mantle convection for Earth and why other planets including Mars and Venus have stagnant lid mantle convection without plate tectonics [e.g., *Bercovici*, 2003]. Mantle convection modeling studies show that low lithospheric yield stress (~100–200 MPa) or small coefficient of friction (0.03–0.13) is the key to producing plate tectonics-like surface motions [e.g., *Moresi and Solomatov*, 1998; *Tackley*, 2000; *Lenardic et al.*, 2003; *Van Heck and Tackley*, 2008; *Foley and Becker*, 2009]. While the required low lithospheric yield strength seems consistent with the reduced lithospheric strength for plate boundaries and faults [e.g., *Kanamori*, 1980], it is contradictory with >500 MPa yield stress from laboratory studies [e.g., *Kohlstedt and Mackwell*, 2009], some flexural loading studies [e.g., *Watts*, 2001], and in situ borehole measurements of the frictional coefficient of 0.6 [e.g., *Zoback and Townend*, 2001].

[6] The goal of this study is to constrain lithospheric rheology and stress by modeling the vertical displacement induced by volcanic loading associated with the emplacement of the Hawaiian Islands on the interior of the Pacific plate and comparing the modeled displacements with the observed. We use three-dimensional finite element loading models that include realistic viscoelasticity and lithospheric rheology constrained by recent laboratory studies (Figure 1), i.e., the yielding governed by the Byerlee's law and low-temperature plasticity flow law [e.g., *Mei et al.*, 2010]. The paper begins by reviewing the pertinent laboratory experiments on mantle rheology at lithospheric conditions and the relevant geophysical observations of lithospheric deformation in the region of the Hawaiian Islands volcano loads. We then describe the

loading model, the numerical methods, and the loads. Finally, we compare the observed and calculated deformation in an attempt to constrain mantle rheology in the interior of an oceanic lithospheric plate.

2. Lithospheric Rheology From Laboratory and Field-Based Studies

2.1. Laboratory Studies

[7] Laboratory studies suggest that rock deformation at lithospheric conditions (i.e., for temperatures <1100°C) operates at three different regimes: brittle or frictional sliding, semi-brittle, and plastic flow (Figure 1) [e.g., *Kohlstedt et al.*, 1995]. At shallow depths and low temperatures, deformation involves frictional sliding and the shear stress/strength τ at which frictional sliding occurs is related to the normal stress σ_n as (Figure 1) [e.g., *Byerlee*, 1978; *Kohlstedt et al.*, 1995]:

$$\tau = \mu_f \sigma_n + C_f, \tag{1}$$

where μ_f is the coefficient of friction ranging from 0.6 to 0.85 and C_f is the frictional cohesive strength. When pore fluids are present, pore pressure may reduce the shear strength by reducing the effective normal stress [e.g., *Kohlstedt et al.*, 1995].

[8] At relatively high temperatures (> ~400°C), mantle deformation may be dominated by plastic flow which is controlled by dislocation glide that is resisted by lattice friction (i.e., the Peierls stress) for temperatures < ~800°C (i.e., low-temperature plasticity) and by dislocation and diffusion creep for temperatures > ~800°C (i.e., high-temperature creep) [e.g., *Mei et al.*, 2010]. The flow law for low-temperature plasticity is given by an exponential law equation [*Evans and Goetze*, 1979; *Mei et al.*, 2010]:

$$\dot{\varepsilon} = A\sigma^n \exp\left\{-\frac{E_p}{RT}\left[1-\left(\frac{\sigma}{\sigma_p}\right)^p\right]^q\right\}, \tag{2}$$

where $\dot{\varepsilon}$, σ, T, and R are the strain rate, stress, temperature, and gas constant, respectively, σ_p is the Peierls stress or glide resistance, and E_p is activation energy for dislocation gliding. Early studies used indentation experiments on olivine single crystal and aggregates for temperatures up to 700°C [*Evans and Goetze*, 1979]. Recent developments include relaxation experiments in DIA apparatus at high pressure for temperature from 500 to 890°C by *Raterron et al.* [2004] and steady state experiments in deformation DIA for temperature from 400 to 1000°C by *Mei et al.* [2010]. These studies yield quite different flow laws with the weakest and strongest lithospheric strength reported by *Raterron et al.* [2004] and *Mei et al.* [2010], respectively (Figure 1). A recent study of triaxial compression experiments on olivine single crystals by *Demouchy et al.* [2013] also suggested a relatively low strength for lithosphere compared with previous studies.

[9] The dislocation and diffusion creep at high temperatures is well described by the power law that in its simplest form is given by

$$\dot{\varepsilon} = A\sigma^n \exp\left(-\frac{E_c}{RT}\right), \tag{3}$$

where n is the power law exponent which is 1 for diffusion creep and 3–3.5 for dislocation creep, E_c is the activation energy for creep and is ~500 KJ/mol for various conditions, and pre-exponential factor A depends on pressure, grain size, and the volatile content [e.g., *Hirth and Kohlstedt*, 2003; *Karato and Jung*, 2003].

[10] The semi-brittle deformation regime is a transitional regime between the frictional sliding and low-temperature plasticity, and it limits the lithospheric strength as predicted by frictional sliding and low-temperature plasticity. However, the semi-brittle deformation regime is not well understood. *Kohlstedt and Mackwell* [2009] pointed out that the semi-brittle deformation initiates when the plastic flow strength is about five times of the frictional strength, which is referred to as the brittle-ductile transition (BDT). As depth/pressure and temperature increase, brittle deformation is prevented and the semi-brittle deformation switches to fully plastic flow, which defines the brittle-plastic transition (BPT) [*Kohlstedt and Mackwell*, 2009]. The BPT is determined by the Goetze criterion (Figure 1) [*Kohlstedt et al.*, 1995; *Kohlstedt and Mackwell*, 2009]. *Mei et al.* [2010] suggested that the BPT occurs at shallower depths for weaker flow law for low-temperature plasticity (Figure 1). However, between the BDT and BPT, neither the lithospheric strength nor deformation mechanism is well defined [*Kohlstedt and Mackwell*, 2009].

[11] Water may also have an important effect on lithospheric rheology, as suggested by laboratory studies [e.g., *Hirth and Kohlstedt*, 1996]. The melting process at the mid-ocean ridge that produces the oceanic crust, for example, may leave the melt residue layer (i.e., approximately the top 80 km) dehydrated with a factor of 10 and higher increase in viscosity, compared to undepleted mantle under the same conditions [*Hirth and Kohlstedt*, 1996]. On the other hand, hydration of oceanic lithosphere may reduce its strength [*Ranero et al.*, 2003; *Ruepke et al.*, 2009; *Katayama and Karato*, 2008].

2.2. Field-Based Studies

[12] Surface observations such as topography, the gravitational field, and the seismic structure provide independent constraints on lithospheric rheology and are therefore potentially of great importance in calibrating laboratory work. The viscosity of the upper mantle including the asthenosphere is < ~10^{21} Pa s, as constrained by postglacial rebound and postseismic deformation processes that operate on time scales of 1–10^5 years [*Peltier*, 1998; *Mitrovica and Forte*, 1997; *Paulson et al.*, 2007; *Freed et al.*, 2010]. The lithosphere, due to its lower average temperature, is expected to be much more viscous than the asthenosphere. Therefore, in order to constrain lithospheric rheology, one must rely on observations associated with long-term (>10^6 years) geological loads such as those associated with erosion, sedimentation, volcanism, rifting, and mountain building [*Watts*, 1978; *McNutt*, 1980].

[13] The Earth's response to long-term loads is usually modeled as a thin elastic plate that overlies an inviscid fluid (i.e., zero viscosity) [e.g., *Watts*, 2001]. By comparing the surface topography and gravity or geoid anomaly to the predictions of an elastic plate model, it is possible to determine the flexural rigidity or elastic plate thickness of the lithosphere in the vicinity of a load [e.g., *Watts*, 1978; *Forsyth*, 1985]. Oceanic flexural studies suggest that the elastic thickness is controlled by the thermal structure of the lithosphere at the time of loading and given approximately by the depth to the ~450°C isotherm based on cooling plate models. The elastic thickness increases from ~10 km to 40 km as the age of the lithosphere increases [e.g., *Watts et al.*, 1980]. For

example, at the Hawaiian Islands, which are 0–5 Ma old and have loaded 85–92 Ma oceanic lithosphere, the elastic thickness is ~30 km [e.g., *Watts et al.*, 1980; *Wessel*, 1993]. The elastic thickness is significantly less (~10 km) at similar age volcanoes such as the Azores that have loaded lithosphere of 10 to 12 Ma [*Luis and Neves*, 2006]. Irrespective of thermal structure, the elastic thickness may be reduced significantly in high-curvature regions such as the outer rise seaward of trenches [e.g., *Judge and McNutt*, 1991; *Billen and Gurnis*, 2005; *Contreras-Reyes and Osses*, 2010] where there is observational evidence of yielding through faulting.

[14] Despite the orders of magnitude differences in loading times, it is important to attempt to relate the rheological properties of the lithosphere derived from field-based observations such as the elastic thickness to those derived from laboratory studies [e.g., *Goetze and Evans*, 1979]. That the elastic thickness is controlled by lithospheric thermal structure is broadly consistent with thermally controlled rheologies such as those described in equations (2) and (3). The deviatoric stress up to ~500 MPa predicted near oceanic islands and seamounts from the elastic plate model [e.g., *Watts*, 2001] is in general agreement with the lithospheric strength from laboratory studies (e.g., Figure 1). However, the elastic plate model is insufficient in characterizing lithospheric rheology for two reasons. First, the model does not consider the depth-dependent frictional strength or Byerlee's law. Second, the model ignores load-induced, time-dependent, viscous stress relaxation and so is unable to describe the rate of deformation and viscosity. However, loading models with linear viscoelastic rheology (e.g., $n = 1$ in equation (3)) have shown that oceanic elastic thicknesses values can be explained by an activation energy E_c in the range of 120–250 KJ/mol [*Watts et al.*, 2013; *Watts and Zhong*, 2000; *Courtney and Beaumont*, 1983; *Willett et al.*, 1985].

[15] Other constraints on lithospheric rheology have come from studies of long-term processes associated with plate motions and mantle-lithosphere interactions. For example, *Asaadi et al.* [2011] have shown that the shape of the Hawaiian topographic swell requires a non-Newtonian mantle rheology. *van Hunen et al.* [2005] have shown that explaining the seismic results of the Pacific upper mantle [*Ritzwoller et al.*, 2004] with sublithospheric small-scale convection requires an activation energy E_c for the lower lithosphere of 120 KJ/mol for diffusion creep with $n = 1$ or ~360 KJ/mol for dislocation creep with $n = 3.5$.

[16] In order to constrain lithospheric rheology more effectively, we therefore need to reformulate the flexure model to include nonlinear rheological properties including the Byerlee's law and low-temperature plasticity (i.e., equations (1) and (3)), which were ignored in previous studies [e.g., *Watts*, 2001; *Watts and Zhong*, 2000]. By comparing the calculated deformation of the Pacific plate caused by the Hawaiian Islands volcanic loads, using the newly formulated models, to observations of seismically constrained depth to the top of the oceanic lithosphere, we should then be able to constrain mantle rheology.

3. Nonlinear Viscoelastic Loading Models and Hawaiian Island Loads

[17] This section presents a model formulation for determining flexures induced by loads on a viscoelastic lithosphere and mantle, discusses numerical solution procedures, and describes the construction of a volcanic loading history model for the Hawaiian Islands region.

3.1. A Finite Element Model for Load-Induced Deformation in a Viscoelastic Medium

3.1.1. Governing Equations and Boundary Conditions

[18] The response of an incompressible, viscoelastic medium to loads can be described by the conservation laws of mass and momentum [e.g., *Wu*, 1992]. Here we follow the formulation for loading problems in *Zhong* [1997]. The governing equations are

$$u_{i,i} = 0, \tag{4}$$

$$\sigma_{ij,j} - (\rho_0 g u_3)_{,i} = 0, \tag{5}$$

where u_i is the displacement, σ_{ij} is the stress tensor, ρ_0 and g are the background mantle density and gravitational acceleration, and u_3 is the vertical component of the displacement. The second term in (5) represents the restoring force at density interfaces such as the top surface of the deformed plate. We use notation such that $A_{,i}$ represents the derivative of variable A with respect to x_i, and repeated indices indicate summation over those indices.

[19] Our loading model is modified from a three-dimensional (3-D) spherical shell model which was used by *Zhong et al.* [2003] in their studies of postglacial rebound. The model is applicable to different coordinate systems including 2-D Cartesian, 2-D axisymmetric, 3-D Cartesian, and regional spherical geometries. For the loading calculations presented here, the model is set up for a 3-D Cartesian box. The boundary conditions for the bottom of the box at $z = 0$ and the four sidewalls of the box are free slip (i.e., zero shear stress and zero normal displacement), while the top boundary is treated as a deformable free surface that is subjected to time-dependent loads

$$\sigma_{ij} n_j = \sigma_L(x, y, t) n_i, \tag{6}$$

where n_i is the normal vector of the top surface and $\sigma_L(x,y,t)$ represents the pressure produced by the loads (e.g., volcanic material) at the surface at location (x,y) and time t.

3.1.2. Rheological Equations

[20] The rheological equation for an incompressible Maxwellian media is given by [e.g., *Zhong et al.*, 2003]

$$\sigma_{ij} + \frac{\eta}{\mu}\frac{d\sigma_{ij}}{dt} = -p\delta_{ij} + \eta\frac{d\varepsilon_{ij}}{dt}, \tag{7}$$

where η and μ are the viscosity and shear modulus, respectively, p is the dynamic pressure, δ_{ij} is the Kronecker delta function, and ε_{ij} is the strain tensor that includes both elastic and viscous strains and is related to displacement u_i as $\varepsilon_{ij} = (\partial u_i/\partial x_j + \partial u_j/\partial x_i)/2$ [*Zhong et al.*, 2003].

[21] In this study, we incorporate a nonlinear rheology for the lithosphere and mantle: Byerlee's law, low-temperature plasticity, and high-temperature creep flow (i.e., equations (1)–(3)), while assuming a relatively simple model for shear modulus that is either constant or only dependent on depth. The high-temperature creep flow law is approximated by a composite power law rheology that combines both diffusion and dislocation creep [e.g., *Hirth and Kohlstedt*, 2003]. A simplified form of this flow law where the activation energy

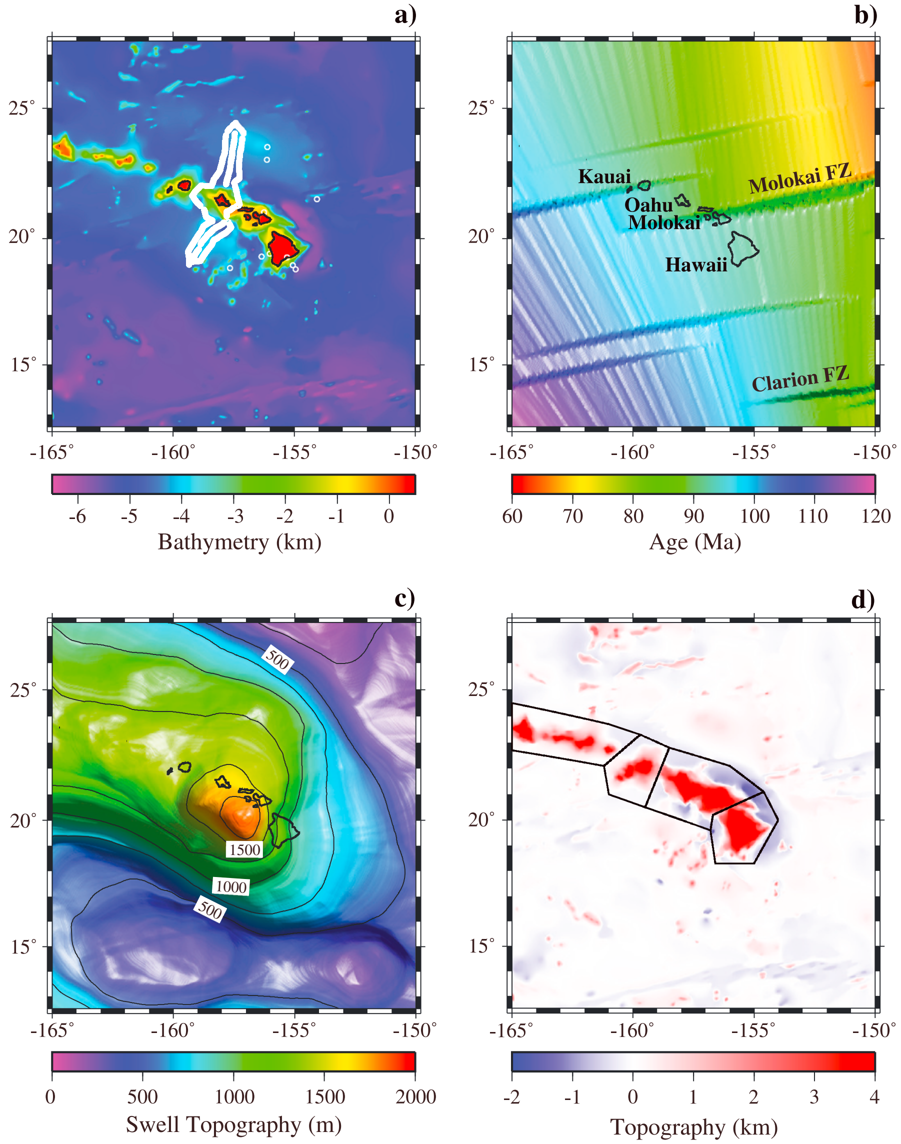

Figure 2. (a) Bathymetry, (b) seafloor age, (c) swell topography from a median filter, and (d) residual topography (i.e., volcanic loads) after corrections for swell topography and thermal isostasy. The white circles in Figure 2a indicate locations where seismic constraints exist on the top and bottom of oceanic crust (i.e., flexures). The contour interval in Figure 2c is 250 m. Figure 2d only shows the loads below the sea level, and the line segments in Figure 2d outline four regions with each region that covers a loading stage (see Table 1). The seafloor age plotted in Figure 2b is for version 3.2, but the age used in model calculations is from version 1.6 [*Muller et al.*, 1997]. However, our model results are insensitive to the difference between versions 1.6 and 3.2 [*Muller et al.*, 1997, 2008].

E_c is the same for both creep mechanisms is given by [*Podolefsky et al.*, 2004]

$$\eta = \frac{A_f}{1+(\sigma/\sigma_{\mathrm{tran}})^{n-1}} \exp\left(\frac{E_c}{RT}\right), \tag{8}$$

where η is the effective viscosity, σ is the second invariant of deviatoric stress tensor, σ_{tran} is the transition stress between dislocation and diffusion creep, and A_f is a pre-exponential factor that includes the effects of grain size and water content. We ignore the pressure dependence in viscosity. This is justified for the long-term loads in this study because the mantle viscosity in the lithosphere (i.e., at relatively small pressure) is more important than the mantle viscosity in the asthenosphere. We assume $n = 3.5$, unless otherwise indicated. Therefore, the three main controlling rheological parameters for high-temperature creep are activation energy E_c, transition stress σ_{tran}, and pre-exponential factor A_f. Given that the stress in the asthenosphere is small and temperature is nearly constant at $T_m = 1623$ K (i.e., 1350°C), the pre-exponential factor A_f can be expressed in terms of the reference asthenospheric viscosity η_0 as

$$\eta_0 = A_f \exp\left(\frac{E_c}{RT_m}\right). \tag{9}$$

Equation (8) can then be rewritten as

$$\eta = \eta_0 \frac{1}{1 + (\sigma/\sigma_{\text{tran}})^{n-1}} \exp\left(\frac{E_c}{RT} - \frac{E_c}{RT_m}\right). \tag{10}$$

[22] For low-temperature plasticity, the exponential flow law may have different forms [e.g., *Mei et al.*, 2010]. In this study, we consider four published flow laws [*Mei et al.*, 2010; *Raterron et al.*, 2004; *Katayama and Karato*, 2008; *Evans and Goetze*, 1979], but we use the flow law by *Mei et al.* [2010] (i.e., $n=2$, $p=1/2$, and $q=1$ in equation (2)) as an example in the following discussion. The effective viscosity based on *Mei et al.* [2010] can be expressed as

$$\eta = \frac{\sigma}{\dot{\varepsilon}} = \frac{1}{A_t \sigma} \exp\left[\frac{E_p}{RT}\left(1 - \sqrt{\frac{\sigma}{\sigma_p}}\right)\right], \tag{11}$$

where A_t, E_p, and σ_p are the pre-exponential factor, activation energy, and Peierls stress, respectively, and are experimentally determined and listed in the respective publications.

[23] For Byerlee's law (i.e., equation (1)), we use a simplified form

$$\tau_y = \mu_f \sigma_n, \tag{12}$$

where τ_y is the frictional strength or yield stress and the normal stress σ_n is assumed to be hydrostatic pressure that includes the load pressure. The effective viscosity in the frictional sliding regime is

$$\eta = {}^{\tau_y}\!/_{\dot{\varepsilon}}, \text{for } \sigma > \tau_y. \tag{13}$$

[24] In practice, for temperatures greater than a threshold (i.e., 800°C), equation (10) for high-temperature creep is used to determine the effective viscosity, and different threshold temperatures are also used to test its effects. At temperatures lower than the threshold, the effective viscosity is taken as the smaller of those predicted from equations (11) and (13) for low-temperature plasticity and Byerlee's law. However, no threshold temperature is set for the transition between the low-temperature plasticity and frictional sliding regimes, and the transition is dynamically determined by equations (11) and (13). Because no flow law is available for the poorly understood semi-brittle regime [e.g., *Kohlstedt and Mackwell*, 2009], semi-brittle deformation is approximated by low-temperature plasticity and frictional sliding deformation (i.e., equations (11) and (13)) and is not explicitly considered in our models. However, this approximation is justified and does not introduce significant error into our model results as will be discussed later. Because the frictional strength (i.e., yield stress τ_y) is generally large at large depths, the effective viscosity of lithosphere at temperatures below 800°C is mostly determined by low-temperature plasticity.

3.2. Models of Hawaiian Volcanic Loads and Lithospheric Thermal Structure

[25] The Hawaiian volcanic island chain (Figure 2a) formed over the last tens of Ma as the Pacific plate moves westward above a thermal plume [*Morgan*, 1971] which appears to have been fixed with respect to the deep mantle for at least the last ~40 Myr [*Tarduno et al.*, 2003]. The big island, Hawaii, the youngest island in the chain was formed in the last million years on ~80 Ma old seafloor (Figure 2b). The volcanic loads that comprise the chain have been derived from the present-day bathymetry and vary in time and space. Here we describe the steps with which the loads are derived.

3.2.1. Spatial Pattern of Volcanic Loads

[26] We use a GEBCO 1 × 1 minute bathymetric grid data for a 30° × 30° region (5°N to 35°N and 187.5°E to 217.5°E). The grid was resampled onto a grid with a resolution of 1/30° and the resultant data are used for the analysis. In order to construct a model of the volcanic loads, we need to first separate other contributions to topography such as those associated with thermal isostasy and the dynamics of the Hawaiian plume. Thermal isostasy can be corrected for by consideration of the age of the seafloor and the plate cooling models. The Hawaiian plume is associated with a topographic swell ~1.2 km high and ~1000 km wide (Figure 2a) that probably results from the isostatic compensation of the plume buoyancy near the base of the lithosphere [e.g., *Davies*, 1988; *Olson*, 1990; *Ribe and Christensen*, 1994]. Both the thermal isostasy-induced topography and the swell topography have a distinctly larger length scale than the topography associated with the volcanic loads and loading process which simplifies their removal from bathymetric data.

[27] To remove thermal isostasy effects, we use an ocean depth-age relation that was derived from an analysis of North Pacific bathymetry by *Hillier and Watts* [2005]:

$$\begin{aligned} d &= 3010 - 307 t_s^{1/2}, \quad \text{for } t_s \le 85\,\text{Ma}, \\ d &= -6170 + 3010 \exp(-0.026 t_s), \quad \text{for } t_s > 85\,\text{Ma}, \end{aligned} \tag{14}$$

where d is the ocean depth in meters and t_s represents the seafloor age and is taken from *Muller et al.* [1997] (Figure 2b). *Hillier and Watts* [2005] analyses differ from previous analyses [e.g., *Stein and Stein*, 1992] in that seamounts and oceanic islands were removed with a filter. Hillier and Watts' results are confirmed by *Zhong et al.* [2007b] who used different methods to remove these topographic effects. To remove the Hawaiian topographic swell, we applied a 500 km median filter, similar to *Hillier and Watts* [2005], and we found this filter width to be effective in removing the swell topography (Figure 2c).

[28] The topography after removal of thermal isostasy and swell effects shows large, positive features, representing the surface loads associated with the volcanic chain constructs and flanking negative topography, representing the flexural depressions caused by these loads. The resulting residual topography is approximately zero at large distance from the island chain (Figure 2d). The residual topography map is used to build the loads $\sigma_L(x,y,t)$ that are required in equation (6). The loads $\sigma_L(x,y,t)$ consist of two parts: so-called "static" loads $\sigma_{\text{LS}}(x,y,t)$ and "dynamic" loads $\sigma_{\text{LD}}(x,y,t)$. We divide the island chain into four different regions, shown in outline in Figure 2d. Positive topography in these regions is considered as the static part of volcanic loads $\sigma_{\text{LS}}(x,y,t)$. Volcanic loads flex the lithosphere and produce significant subsidence below the loads and their close proximity and moderate uplift at some intermediate distance. Because of the way that submarine volcanoes evolve, we should expect that the subsidence would be filled with the same volcanic rocks as the loads immediately beneath the loads and with volcanoclastic and pelagic sediments in surrounding regions. These infills of the flexural depressions form the dynamic part of the loads σ_{LD}

Table 1. A Five-Stage Loading History Model

Stage	t_B (Ka)[a]	t_E (Ka)[a]	Loading Region[b]
1	2150.6	2125.3	1
2	2125.3	2100	2
3	2100	1100	3
4	1100	100	4
5	100	0	-

[a] t_B and t_E are the beginning and ending times for each loading stage in thousand years (Ka) before the present.

[b] Loading regions are specified in Figure 2d and are numbered as regions 1, 2, 3, and 4 from west to east. For the fifth stage, no new loads are added.

(x,y,t). We refer to the infills as dynamic loads, because the depression induced by the loads depends on the mechanical structure of the lithosphere. Therefore, the dynamic loads $\sigma_{\rm LD}(x,y,t)$ comprise the volcanic rock infill between the depressed surface and the base of the static volcanic loads in the region of the volcanic loads and the sediment infill between the depressed surface and the corrected topography in Figure 2d outside of the volcanic loads [e.g., *Watts and ten Brink*, 1989].

3.2.2. Temporal Pattern of Volcanic Loads and Loading History

[29] The Hawaiian volcanic island chain has been emplaced on the Pacific plate over a period of several million years. The further east an island is, the younger it is. For example, Hawaii formed within the last million years [*Moore and Clague*, 1992], while the shield to post-shield building phase on Molokai was between 2 Ma and 1 Ma ago, and on Oahu between 4 and 2 Ma ago [*Clague and Dalrymple*, 1988]. Because the precise history of volcanic island building is not well constrained (e.g., the shield building times) [e.g., *Moore and Clague*, 1992], we use a simplified loading history in which the loading takes place in five time stages over a total of 2.1 Ma (Table 1). The loads in each of the four regions in Figure 2d are applied over a certain period of time with one stage following the other, starting from region 1 for the oldest islands. In each loading stage, the loads are assumed to increase linearly with time from zero to their full amplitude as constrained by the residual topography map (e.g., Figure 2d). The final loading stage for the last 100 Ka does not include any new loads.

[30] The total loading time of 2.1 Ma over the five stages is significantly shorter than the likely island-building time, particularly for the first two stages for the old islands (Table 1). However, the loading times for Hawaii between 0.1 and 1.1 Ma ago and for Molokai from 2.1 Ma to 1.1 Ma ago are generally consistent with observations [*Moore and Clague*, 1992; *Clague and Dalrymple*, 1988]. The loading time for Oahu, which has been grouped together with Molokai in the same loading stage (Figure 2d, and Table 1), is however clearly an approximation [*Clague and Dalrymple*, 1988]. The shortened loading time is used to reduce computational cost. However, since we only model the present-day flexures (i.e., the top of oceanic crust) near Hawaii, Oahu, and Molokai, the details in loading history including the shortened loading time do not affect our results, as will be discussed in a later section.

3.2.3. Lithospheric and Mantle Thermal Structure

[31] The temperature field is the key for constraining viscosity, hence lithospheric rheology (e.g., equations (2) and (3)). In this study, we assume a cooling half-space model for computing the lithospheric and mantle temperature [e.g., *Turcotte and Schubert*, 2002],

$$T = T_o + (T_m - T_o)\,\mathrm{erf}\left(\frac{y}{2\sqrt{\kappa t_s}}\right), \qquad (15)$$

where erf stands for the error function, y is the depth, t_s is the crustal age, κ is thermal diffusivity, and T_m and T_o are the mantle and surface temperatures, respectively (Table 2).

[32] A number of assumptions and potential complications need some discussion. First, the mantle plume is likely to modify the mantle and lithospheric thermal structure predicted by equation (15) [e.g., *Ribe and Christensen*, 1994]. However, both mantle dynamic modeling and surface heat flow and elastic thickness observations have shown that the plume may not affect either the thermal or mechanical structure of the uppermost part of the lithosphere (i.e., the top 50–70 km) at Hawaii [*Ribe and Christensen*, 1994; *Zhong and Watts*, 2002; *von Herzen et al.*, 1989]. Because our loading model is mostly sensitive to the thermal structure of the upper lithosphere, this suggests that the cooling half-space model is generally applicable. Second, we assume that the effects of magma and melts on the lithospheric thermal structure are small and can be ignored. Third, the lithospheric thermal structure estimated from present-day crustal age (Figure 2b) is assumed for the entire loading period and therefore ignores the fact that the lithosphere was younger and probably hotter when the volcanic island loads were first emplaced on the surface. However, since we are only

Table 2. Model Parameters

Parameter	Value
Mantle temperature, T_m	1350°C
Shear modulus, μ	0.333×10^{11} Pa
Thermal diffusivity, κ	10^{-6} m^2/s
Gravitational acceleration, g	9.8 m/s^2
Gas constant, R	8.32 J/(mol K)
Mantle density, ρ_0	3330 kg/m^3
Crustal density, $\rho_{\rm c}$	2800 kg/m^3
Water density, $\rho_{\rm w}$	1030 kg/m^3
Rock infill density, $\rho_{\rm rk}$	2800 kg/m^3
Sediment infill density, $\rho_{\rm sd}$	2300 kg/m^3
High-temperature creep rheology (*equation* (10))	
Power law exponent, n	3.5
Activation energy, E_c[a]	360 KJ/mol
Transition stress, $\sigma_{\rm tran}$[a]	3×10^5 Pa
Asthenospheric viscosity, η_0[a]	10^{20} Pas
Low-temperature plasticity (*equation* (11) *for Mei et al*. [2010])	
Activation energy, E_p	320 KJ/mol
Prefactor, A_t[a]	1.4×10^{-7} s^{-1} MPa^{-2}
Peierls stress, σ_p	5.9 GPa
Other low-temperature plasticity flow laws	
Katayama and Karato [2008]:	
$\dot{\varepsilon} = 10^{7.8}\sigma^2 \exp\left\{-5.18 \times 10^5[1-(\sigma(\mathrm{GPa})/2.87)]^2/(RT)\right\}$	
Raterron et al. [2004]:	
$\dot{\varepsilon} = 2.6 \times 10^{16} \exp\left\{-5.64 \times 10^5\left[1-(\sigma(\mathrm{GPa})/15.4)^{2/3}\right]^2/(RT)\right\}$	
Evans and Goetze [1979]:	
$\dot{\varepsilon} = 1.3 \times 10^{12} \exp\left\{-4.99 \times 10^5[1-(\sigma(\mathrm{GPa})/9.1)]^2/(RT)\right\}$	

[a] These parameters are varied in model calculations to examine their sensitivity.

interested in the regions with young volcanism (<~4 Ma), the time dependence in lithospheric thermal structure is not expected to affect our results significantly.

3.3. A 3-D Cartesian Finite Element Model

[33] The governing equations (4) and (5) with the viscoelastic rheological equation (7) can be solved analytically if both shear modulus μ and viscosity η are the only depth-dependent variables, as for postglacial rebound [e.g., *Peltier*, 1998] or long-term crustal and lithospheric deformation studies [*Zhong*, 1997]. However, if μ or η is laterally variable due to a nonlinear rheology or lateral temperature variations, numerical solutions are needed, for example, a finite element method in postglacial rebound studies [e.g., *Zhong et al.*, 2003]. In this study, we modified the finite element code in *Zhong et al.* [2003] to incorporate nonlinear rheological equations (10), (11) and (13) in a 3-D Cartesian model.

[34] Most of the details of the finite element analyses including a variational form for the finite element formulation and time discretization of the rheological equation (7) can be found in *Zhong et al.* [2003]. For the nonlinear rheology assumed in this study, we use an iterative scheme in which at each time step, the effective viscosity is updated iteratively using an updated stress field, until the relative change in displacement field is less than 1%, similar to that used in modeling mantle convection with nonlinear viscosity [e.g., *Zhong et al.*, 1998].

[35] Benchmark calculations have been performed to validate the finite element code for surface loading of a viscoelastic medium with depth-dependent viscosity for which analytical solutions of the time-dependent surface deformation are available for comparison [*Zhong*, 1997]. The benchmark results (Appendix A) demonstrate the effectiveness of our finite element loading models.

[36] The spatial domain of the model corresponds to the 15°×15° region of the study area, as depicted in Figure 2 (i.e., 12.5°N to 27.5°N and 195°E to 210°E). By using the Cartesian box model, we ignore the spherical geometry effect. We use the following coordinate transformation to map the longitude ϕ and latitude θ to Cartesian coordinates x and y:

$$\begin{aligned} x &= R(\phi - \phi_1)\pi/180\cos\theta_2, \\ y &= R(\theta - \theta_1)\pi/180, \end{aligned} \tag{16}$$

where $\theta_1 = 12.5°\mathrm{N}$ and $\phi_1 = 195°\mathrm{E}$ which specify the coordinates for the left lower corner of the model domain and are mapped to $x=0$ and $y=0$, $R=6370$ km, and $\theta_2 = 27.5°\mathrm{N}$ is the latitude of the northern boundary of the model domain. As a result, the 3-D Cartesian box of our model is 1479.23 km and 1667.66 km in length in the x (i.e., east-west) and y (i.e., north-south) directions, respectively. The box is 500 km in depth, covering only the upper mantle. The model box is sufficiently large such that the results are not sensitive to the box size.

[37] The model uses 32 elements in a vertical direction and 192 elements in each of the horizontal directions. The grid is significantly refined in the vertical direction with 5 km per element for the top 50–80 km of the model (i.e., the upper lithosphere). Such a numerical resolution is found sufficient to define the loads and to resolve the deformation. The model uses a uniform time step $\Delta t = ct_\mathrm{M}$, where c is a constant fraction (e.g., 0.25) and $t_\mathrm{M} = \eta_0/\mu$ is the Maxwell time of the upper mantle, where η_0 is the reference asthenospheric viscosity as in equation (9) and μ is the mantle shear modulus (Table 2). In our study, η_0 is chosen to be 10^{20} Pa s for most cases in deriving mantle viscosity for high-temperature creep flow in equation (10). However, this would lead to $t_\mathrm{M} \sim 100$ years and even smaller time step Δt, making the modeling computationally expensive. Since the stress in the upper mantle with ~10^{20} Pa s viscosity should be largely relaxed on the time scales of 1 Ma as in our models, the relevant stress relaxation should be focused within the lithosphere [e.g., *Watts and Zhong*, 2000]. To circumvent the difficulty, we impose a lower limit on the upper mantle viscosity at 10^{21} Pa s and use $\Delta t = ct_\mathrm{M1}$ where $t_\mathrm{M1} \sim 1000$ years is the Maxwell time determined by 10^{21} Pa s. Our numerical tests show that this procedure does not affect the stress relaxation in the upper lithosphere while significantly reducing the number of time steps needed and hence computational cost.

4. Observations of Load-Induced Flexure and Seismicity at Hawaii

[38] Two types of observations are used to constrain our loading models and lithospheric rheology. They are the load-induced flexures of the top of the oceanic crust and seismicity in the Hawaiian region. The flexures of the top of the oceanic crust are now partly obscured by volcanoclastic and pelagic sediments or volcanic rocks (i.e., the infills). The buried, flexed surfaces will still be visible, however, in seismic reflection profiles because of the large acoustic impedance contrast between the infill material and the upper oceanic crust. For example, the Hawaiian seismic experiment (R/V Conrad cruise C2308) included three seismic reflection profiles which intersected the Hawaiian Islands between Oahu and Molokai and seven seismic refraction profiles that linked the reflection profiles [*Watts et al.*, 1985; *Watts and ten Brink*, 1989]. Other constraints on the depth to the top of the oceanic crust have been provided by seismic surveys at various other sites near Hawaii [*Zucca et al.*, 1982; *Zucca and Hill*, 1980; *Shor and Pollard*, 1964]. The seismic data reveal that the top and bottom of normal thickness Pacific oceanic crust is flexed downward from its normal depth by up to a few kilometers and that the amount of flexure systematically increases toward the islands (e.g., Figure 3a). *Watts and ten Brink* [1989] used a subset of the flexure data from the Oahu/Molokai seismic profiles and the data points near Hawaii to determine the elastic thickness in the Hawaiian Islands region to be ~40 km. *Wessel* [1993] reanalyzed the flexure data of the Oahu/Molokai seismic profiles by removing the swell topography and reported an elastic thickness of ~33 km below the loads.

[39] Load-induced surface vertical motions are also apparent in submerged reef data in the vicinity of the Hawaiian Islands. Reefs formed initially at sea level on Molokai and Hawaii are now at depths down to ~1300 m below sea level, and these reefs are dated at ~500 Ka or younger [*Moore and Campbell*, 1987; *Ludwig et al.*, 1991] (Figure 3b for depth locations of six groups of reefs of different ages on the northwest side of Hawaii). These reefs have subsided together with the islands, as the islands grow and new volcanic loads are added to cause the subsidence. Such time-dependent vertical motions provide constraints on the growth history of the

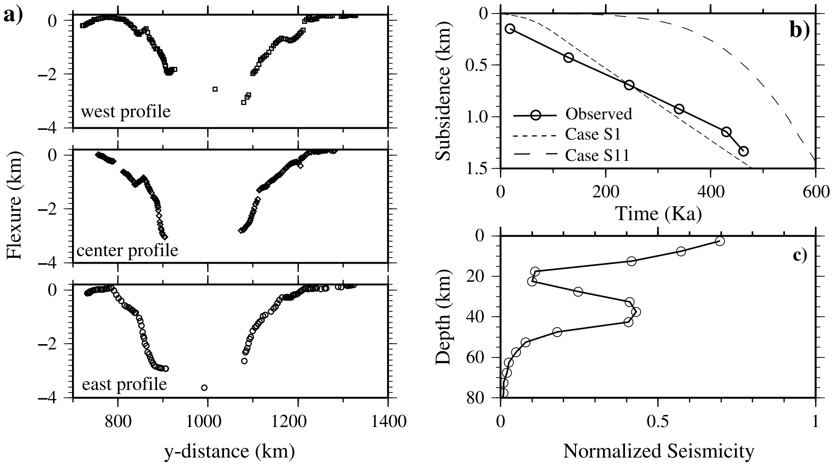

Figure 3. Seismically constrained depths to the top of oceanic crust (i.e., flexures) for the three profiles that intersect the Hawaiian Islands ridge between Oahu and Molokai [*Watts et al.*, 1985] (see Figure 2a) after (a) corrections for swell topography, thermal isostasy, and crustal thickness, (b) subsidence history inferred from submerged reefs northwest of Hawaii [*Moore and Clague*, 1992] and model predictions from two cases, (c) and depth distribution of normalized seismicity [*Anchieta et al.*, 2011].

islands [*Moore and Clague*, 1992] and loading models [*Watts and Zhong*, 2000].

[40] The load-induced lithospheric deformation also manifests itself in seismicity data beneath and around the Hawaiian islands, especially Hawaii [e.g., *Wolfe et al.*, 2004]. The seismicity within ~200 km distance from the center of Hawaii recorded by the PLUME seismic network and in the Hawaiian Volcano Observatory catalog shows a minimum in activity at ~20 km depth and two peaks at crustal (0–15 km) and mantle depths (35–40 km), respectively (Figure 3c) [*Anchieta et al.*, 2011]. The seismicity pattern has implications for the flexure, the stress, and the lithospheric rheology [*Anchieta et al.*, 2011; *Pritchard et al.*, 2007].

[41] In this study, we use the full data set of seismically constrained digitized depths to the top and bottom of oceanic crust (i.e., Reflectors 2 and 3) along the three profiles that intersect the Hawaiian Islands between Oahu and Molokai [*Watts and ten Brink*, 1989] with proper corrections for swell topography, thermal isostasy, and crustal thickness (Figures 2a and 3a). We also used the results of other surveys in the vicinity of Hawaii, notably those of *Zucca and Hill* [1980] and *Zucca et al.* [1982]. The seismically constrained flexures were corrected for thermal isostasy (Figure 2b) and the swell topography (Figure 2c) in the same way as the topography was corrected. For the flexures along the Oahu/Molokai profiles, to reduce the local irregularities due, for example, to intersecting fracture zones, we apply a 10 km window averaging [*Wessel*, 1993], and in the central region of the loads, we only use an averaged flexure [*Watts and ten Brink*, 1989]. For the Oahu/Molokai profiles, we also apply corrections for oceanic crustal thickness variations that were determined from the same seismic experiment (i.e., Reflector 3 from *Watts and ten Brink* [1989]). As discussed in *Watts and ten Brink* [1989], the crustal thickness appears thinner than normal on the north segments of the profiles near the Molokai Fracture Zone, as it is at fracture zones elsewhere [*Detrick and Purdy*, 1980]. We correct for the crustal thickness effect on the flexure due to the islands loads, assuming local Airy isostasy at the time of formation of the seafloor using the following equation:

$$\delta H = (h_c - h)(\rho_0 - \rho_c)/(\rho_0 - \rho_w), \qquad (17)$$

where δH is the correction to the topography, h and h_c are the crustal thickness and its average along the profiles, and ρ_0, ρ_c, and ρ_w are the mantle, crustal, and water densities, respectively (Table 1). The flexures along the Oahu/Molokai profiles after the corrections are shown in Figure 3a, and it is these profiles that have been used to constrain our loading models.

[42] We define a measure of the model fit to the observations as

$$\chi = \sqrt{\sum_{i=1}^{N} (M_i - O_i)^2} \Bigg/ \sqrt{\sum_{i=1}^{N} O_i^2}, \qquad (18)$$

where N is the number of observation sites, i is the index for observation site, and M_i and O_i are model prediction and seismic observations of the flexures at the ith site. There are many more data points for the Oahu/Molokai region than in other regions, and in order to have a balanced assessment of overall misfit, we assign 50% weighting to the Oahu/Molokai sites and 50% weighting to other sites. While the vertical subsidence and uplift history data at the Hawaiian Islands were used to check the loading history models (Figure 3b), they are not used in defining the misfit. In this study, we also seek to constrain lithospheric rheology from the observed seismicity (Figure 3c) by comparing it with our model predictions of lithospheric deformation and stress.

5. Model Results

[43] In this section, we will first present results for simple models that are equivalent to elastic plate models to illustrate the basic physics of the loading process and modeling

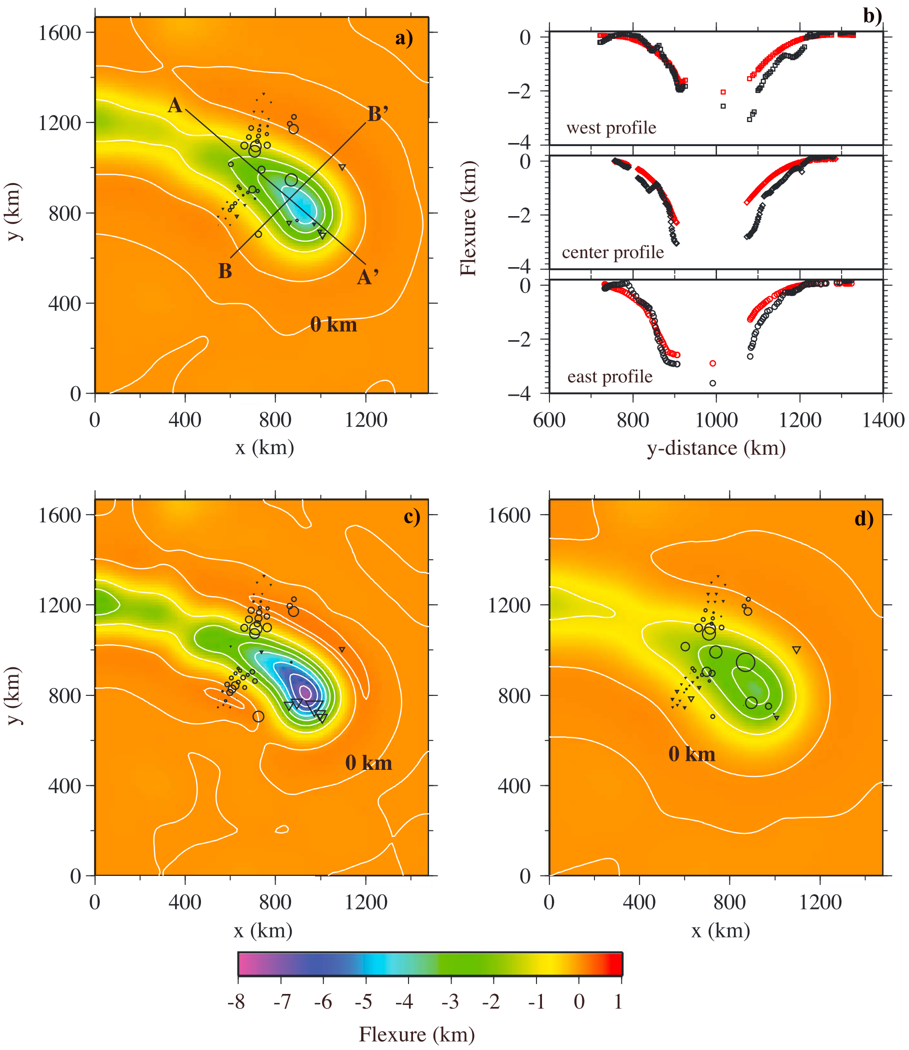

Figure 4. Model prediction (a) of the present-day flexures in a mapview and (b) for the Oahu/Molokai profiles (plotted against y coordinates) for Case S1, and the present-day flexures for Cases (c) S2 and (d) S5. In Figures 4a, 4c, and 4d, the contour levels are 0.1, 0, −1, −2, … in kilometer, and x and y axes are for longitudinal and latitudinal directions, respectively. The symbol represents the difference between the modeled and observed flexure for each site with symbol size as the magnitude of the difference, circles for underpredictions, and triangles for overpredictions. In Figure 4a, the black lines mark cross sections AA' and BB'. In Figure 4b, the red symbols represent the model predictions, while the black symbols are the corresponding observations.

procedures. We will then present models with increasing realism in lithospheric rheology and systematically explore sensitivity of model results to rheological parameters and loading history.

5.1. Simple Models With an Effectively Elastic Plate

[44] These models have two layers of different viscosity: a high-viscosity top layer and a low-viscosity bottom layer, which effectively simulates the classical elastic plate flexure model. The top and bottom layers are assumed to have uniform viscosity of 10^{27} Pa s and 10^{21} Pa s, respectively, that are independent of stress and temperature (i.e., no brittle and nonlinear rheology). For the loading time scale considered here (i.e., several million years), this two-layer model is effectively the same as an elastic plate, in that the high-viscosity top layer supports the loads at the end of the loading process, while the low-viscosity bottom layer with its fast stress relaxation has vanishingly small stress [e.g., *Watts and Zhong*, 2000].

[45] Case S1 has a top layer thickness of 30 km, which is similar to the inferred elastic thickness for Hawaii from the elastic plate model [*Wessel*, 1993]. The flexure for the present-day matches the overall geometry of the loads with the largest flexure of ~5 km occurring beneath Hawaii (Figures 4a and 4b). This predicted flexure compares well with the seismically constrained flexure, although the model in general underpredicts the flexure north of the island chain (Figures 4a and 4b; the size of symbols in Figure 4a represents the amount of deviation). The overall misfit of the predicted flexures for all the sites, as defined in equation (18), is 0.311.

[46] The calculated flexure is time dependent, as the surface loads are applied in five time stages (see section 3.2).

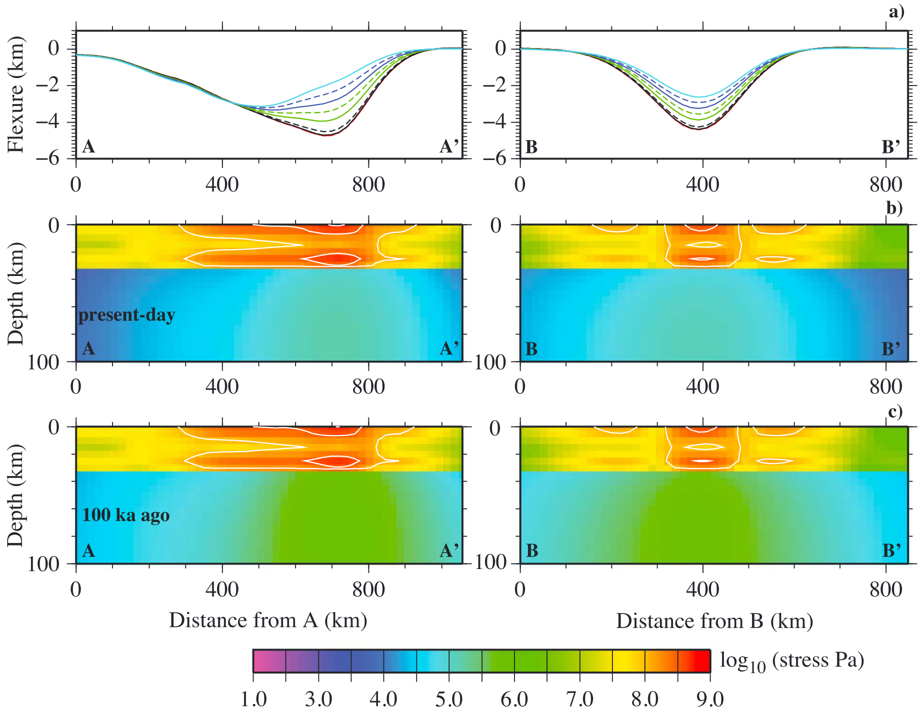

Figure 5. (a) The flexures at 720, 600, 480, 360, 240, and 100 ka ago and at the present day (black solid curves), (b) distribution of the second invariant of stress for the present day and for 100 Ka ago for cross sections AA’ and BB’ (see Figure 4a for their locations) for Case S1. In Figure 5a, the flexures at 120 Ka and 240 Ka into future are also plotted and they overlap with that for the present day. In Figures 5b and 5c, the stress contours are for 100 MPa and 300 MPa.

In the Hawaiian region, the flexures are mostly affected by the fourth stage of loading in which the loads are added continuously as a linear function of time between 1.1 Ma and 100 Ka ago with no new loads added subsequently (Table 1 and Figure 2d). The flexures in the Hawaiian region, as indicated by profiles AA’ and BB’ (see Figure 4a for the profiles’ locations), increase with time as the loads increase (Figure 5a for the present day, 100, 240, 360, 480, 600, and 720 Ka before the present day). However, the change with time in the flexures for the last 100 Ka after the loading ends is negligible.

[47] This temporal pattern in the flexures is controlled by stress relaxation and redistribution in the mantle and plate. As volcanic loads are added to the surface, they introduce stresses in the mantle and plate. The stress in the mantle relaxes relatively rapidly on a time scale of ~10 Ka which is related to the mantle Maxwell time or mantle viscosity of 10^{21} Pa s that is used in our model. However, the high viscosity in the plate leads to a much slower stress relaxation in the plate. Therefore, as the mantle stress relaxes, the stress in the plate will necessarily increase in order to support the loads, and the increased stress in the plate is accompanied by an increase in flexure. For example, at 100 Ka ago when the loading just ended, the stress in the mantle below Oahu/Molokai is $\sim 10^6$ Pa (Figure 5b for the second invariant of the stress tensor along cross sections AA’ and BB’). At the present day, the maximum mantle stress is relaxed to $\sim 10^5$ Pa, while the plate stress and flexure are increased slightly (Figures 5a and 5c). The amplitude of the stress for the present day in Case S1 is high in the plate, reaching up to 300 MPa in localized regions below the major loads (Figure 5c). It should be noted that there is still stress relaxation in the present-day mantle, but because of its small mantle stress ($<10^5$ Pa), the stress relaxation has no discernable effects on the stresses and flexures in the deformed plate (Figure 5a).

[48] Models with plate thicknesses varying from 20 to 60 km (Cases S2–S8 in Table 3) are also computed. A thicker plate leads to a smaller flexure at the present day. Case S2 with a plate thickness of 20 km generally overpredicts seismically constrained flexures significantly, while Case S5 with a plate thickness of 40 km underpredicts them (Figures 4c and 4d). Case S1 with a plate thickness of 30 km yields the minimum misfit value between observed and calculated flexures (Figure 6a). A larger flexure for a thinner plate is accompanied by a larger stress, and the maximum stress is >500 MPa for cases with plate thicknesses <30 km (Figures 7a–7b). It is also noted that for all the cases, lithospheric stress is minimum in mid-plate where the neutral plane is located (e.g., Figures 5b, 7a, and 7b). The magnitude and pattern of stress in the plate are generally consistent with previous studies of loading on an elastic plate [e.g., *Kanamori*, 1980; *Watts*, 2001].

[49] It is important to note here that there are considerable uncertainties with mantle viscosity and the loading history in both its temporal and spatial patterns. It is therefore necessary to explore the effects of these uncertainties on the predicted present-day flexures (e.g., Figures 4a and 4b). Cases S9 and S10 have mantle viscosities of 2×10^{21} Pas and 5×10^{20} Pas, respectively, but otherwise are the same as Case S1 (Table 3). With mantle viscosity that is half of that for Case S1, Case S10 shows nearly identical present-day flexures to Case S1 (Figure 7c for profile AA’ and Table 3 for total misfit). This is expected because with an even smaller mantle

Table 3. Model Parameters and Outputs

Case	Te or High T E_c [b]	η_0 [b](10^{21} Pas)	Low T plasticity[c]	μ_f	Misfit
S1	30 km	1	-	-	0.311
S2	20 km	1	-	-	0.435
S3	25 km	1	-	-	0.339
S4	35 km	1	-	-	0.328
S5	40 km	1	-	-	0.364
S6	45 km	1	-	-	0.404
S7	50 km	1	-	-	0.443
S8	60 km	1	-	-	0.511
S9	30 km	2	-	-	0.306
S10	30 km	0.5	-	-	0.312
S11[a]	30 km	1	-	-	0.315
R1	360 KJ/mol	0.1	M	0.7	0.534
R2	360 KJ/mol	0.1	M_1	0.7	0.492
R3	360 KJ/mol	0.1	M_2	0.7	0.605
R4	240 KJ/mol	0.1	M	0.7	0.532
R5	480 KJ/mol	0.1	M	0.7	0.541
R6	480 KJ/mol	0.01	M	0.7	0.535
R7[b]	480 KJ/mol	0.1	M	0.7	0.533
R8	360 KJ/mol	0.1	EG	0.7	0.420
R9	360 KJ/mol	0.1	R	0.7	0.383
R10	360 KJ/mol	0.1	KK	0.7	0.459
R11	360 KJ/mol	0.1	M(10^2)	0.7	0.503
R12	360 KJ/mol	0.1	M(10^4)	0.7	0.435
R13	360 KJ/mol	0.1	M(10^6)	0.7	0.356
R14	360 KJ/mol	0.1	M(10^8)	0.7	0.295
R15	360 KJ/mol	0.1	M(10^{10})	0.7	0.305
R16[d]	360 KJ/mol	0.1	M(10^8)	0.7	0.291
R17[a]	360 KJ/mol	0.1	M(10^8)	0.7	0.291
R18	360 KJ/mol	0.1	M	0.1	0.472
R19	360 KJ/mol	0.1	M(10^4)	0.1	0.336
R20	360 KJ/mol	0.1	M(10^6)	0.1	0.278
R21	360 KJ/mol	0.1	M(10^4)	0.25	0.398
R22	360 KJ/mol	0.1	M(10^6)	0.25	0.314
R23	360 KJ/mol	0.1	M(10^8)	0.25	0.288

[a] All the cases use a loading history model in which the amplitude of the loads in a given stage grows linearly with time and loading times are listed in Table 1, except for Case S11 in which the load is added eastward and for Case R17 in which the loading times are doubled of those in Table 1.

[b] For high-temperature creep flow law (i.e., equation (10)), all the cases use a transition stress $\sigma_{\text{tran}} = 3 \times 10^5$ Pa except for Case R7 in which $\sigma_{\text{tran}} = 3 \times 10^4$ Pa to enhance the stress weakening effect. E_c is the high-temperature creep activation energy, and η_0 is the asthenospheric viscosity in equation (10). For S models, Te is the thickness of the top high-viscosity layer and η_0 is the viscosity of the mantle below the high-viscosity layer.

[c] For low-temperature plasticity, M, EG, R, and KK represent the flow laws by *Mei et al.* [2010], *Evans and Goetze* [1979], *Raterron et al.* [2004], and *Katayama and Karato* [2008] as defined in Table 2. M_1 differs from M only in using $Ep = 270$ KJ/mol, while M_2 differs from M only in having low-temperature plasticity at temperature less than 1000°C. The number in parentheses is the weakening factor relative to standard [*Mei et al.*, 2010].

[d] Case R16 uses seafloor age of version 3.2.

viscosity than Case S1, mantle stress in Case 10 relaxes rapidly to a diminishingly small level at the present day (i.e., 100 Ka after the loading ended), and as in Case S1, volcanic loads are all supported by the plate. With a larger mantle viscosity and hence slower mantle stress relaxation than Case S1, Case S9 has a larger mantle stress (~10^6 Pa) and smaller plate stress and flexure at the present day than Case 1 does (Figures 7c and 7d), but the difference is small. We believe, therefore, that the uncertainties in the upper mantle viscosity do not affect our results, provided that the upper mantle viscosity is smaller than 2×10^{21} Pas, a condition that is well supported by postglacial rebound studies [e.g., *Paulson et al.*, 2007; *Mitrovica*, 1996].

[50] We point out that Cases S9 and S10 with their different mantle viscosities η_0 can also be interpreted as models with different loading times, because our models are computed in nondimensional quantities and the model time is scaled by the mantle Maxwell time t_M. For example, for Case S1 with $\eta_0 = 10^{21}$ Pas, t_M is ~1000 years and the model computes for ~$2100 t_M$ to cover the total of 2.1 Ma loading time (Table 1). For Cases S9 with $\eta_0 = 2 \times 10^{21}$ Pas and S10 with $\eta_0 = 5 \times 10^{20}$ Pas, the models compute for about $1050 t_M$ and $4200 t_M$, respectively, for the loading time of 2.1 Ma. However, if $\eta_0 = 10^{21}$ Pas is used to define the Maxwell time to scale the time for Cases S9 and S10, then their model times of $1050 t_M$ and $4200 t_M$ would correspond to 1.05 Ma and 4.2 Ma loading times for Cases S9 and S10, respectively. While this rescaling affects the subsidence rate and strain rate (i.e., the time-dependent parameters), it does not affect results for the present-day flexures or stresses. The fact that Cases S9 and S10 produce nearly identical present-day flexures to Case S1 suggests that the shortened loading time of 2.1 Ma (Table 1) should not affect our conclusions that are based on the present-day flexures. We will revisit this loading time issue later for models with realistic thermal and viscosity structures.

[51] Case S11 considers a different spatial pattern in the loading history model but is otherwise identical to Case S1 (Table 3). In Case S11, for each of the four loading stages, the loads are added continuously from west to east, differing from that in Case S1 in which the loads are added at a constant rate throughout the loading region. Figure 7c shows

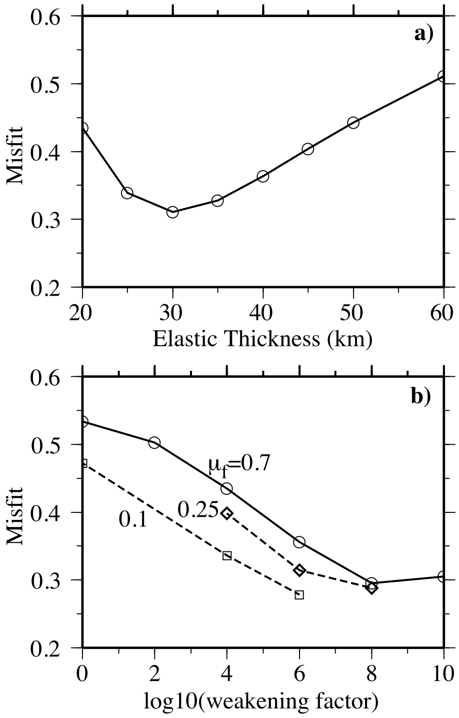

Figure 6. Misfit between the modeled flexures and the seismically constrained depths to the top of oceanic crust (a) for the S models with different elastic thickness and (b) for the R models with different weakening factors and coefficient of friction μ_f (i.e., 0.1, 0.25, and 0.7).

the flexures at 480, 720 Ka ago, and the present day along profile AA' for Case S11 (dashed lines) and their counterparts for Case S1 (solid lines). While the different loading histories give rise to different time-dependent flexures between Cases S11 and S1 during the loading, they are indiscernible at the present day or 100 Ka after the loading ended (the overlapping black dashed and solid curves in Figure 7c). This suggests that different loading histories do not affect the present-day flexures, provided that the loads are added about 100 Ka before the present day—a duration of time during which the relaxation is controlled by the sublithospheric mantle viscosity. This also justifies the significantly shortened loading time for the loads west of Oahu, compared to the ages of those loads (Table 1).

[52] It is also interesting to note that Case S1 reproduces the last 500 Ka subsidence history northwest Hawaii as observed in the submerged reefs, while Case S11 with different loading history predicts too small subsidence for the same period (Figure 3b). Since the total, cumulative subsidence is nearly the same for Cases S1 and S11, there is more subsidence at this site before 500 Ka in Case S11 than in Case S1 (Figure 3b). Clearly, the subsidence history as revealed from the submerged reefs provides important constraints on the Hawaii island-building history [e.g., *Moore and Clague*, 1992]. However, in our current study, we focus on the present-day flexures since these observations are insensitive to loading history. For all the subsequent model calculations, we use the same loading history as in Case S1 (i.e., Table 1) that was demonstrated to reproduce the last 500 Ka vertical motion history at Hawaii. However, we do not use the vertical motion history to constrain the loading models, leaving it for future studies.

5.2. Models With a Reference Lithospheric Rheology

[53] We now consider models that use a realistic lithospheric rheology, namely Byerlee's law, the exponential law creep for low temperatures, and power law creep for high temperatures (i.e., equations (10), (11), and (13)). Lithospheric effective viscosity now is a continuous function of depth due to the temperature-dependent viscosity, different from S cases discussed in the preceding section. Therefore, realistic loading time scales will be required in order to capture the possible stress relaxation in the lithosphere [e.g., *Watts and Zhong*, 2000].

[54] We first describe Case R1 (Table 3) that employs the reference rheological parameters. For high-temperature (i.e., >800°C) creep (equation (10)), the power law exponent n is 3.5, the transition stress $\sigma_{\mathrm{tran}} = 3 \times 10^5$ Pa, the activation energy E_c is 360 KJ/mol, and the reference asthenospheric viscosity η_0 is 10^{20} Pa s. For low-temperature plastic deformation (i.e., <800°C), the rheological equation in *Mei et al.* [2010] (i.e., equation (11)) with $A_t = 1.4 \times 10^{-7}\,\mathrm{s}^{-1}\,\mathrm{MPa}^{-2}$, $E_p = 320$ KJ/mol, and $\sigma_p = 5.9$ GPa was employed. For Byerlee's frictional law (i.e., equation (13)), the frictional coefficient μ_f is set to be 0.7, similar to the standard value from laboratory studies [e.g., *Kohlstedt et al.*, 1995]. In other cases to be discussed later, we will also consider different rheological parameters including E_c (e.g., from 240 to 480 KJ/mol), μ_f (e.g., from 0.7 to 0.1), and different low-temperature plastic deformation laws [e.g., *Evans and Goetze*, 1979; *Raterron et al.*, 2004; *Katayama and Karato*, 2008]. In contrast to the S cases considered in the previous section, the rheological equations (10)–(13) are all highly nonlinear and require an iterative solution in the finite element modeling. Iteration for the nonlinear rheology stops when the relative difference in solutions of displacements between two consecutive iterations is less than 1%. In the model calculation, a minimum mantle viscosity is imposed at 10^{21} Pas, which permits a larger incremental time for each time step (~250 years) and reduces the computational cost. Importantly, the imposed lower bound of mantle viscosity does not affect the model results for the present-day flexure (e.g., Cases S8 and S9).

[55] The calculated present-day flexure for Case R1 is significantly smaller in maximum amplitude than the seismically constrained flexure with an overall misfit of 0.534 (Figures 8a and 8b). The misfit and the flexure are similar to that from a plate with an elastic thickness of >60 km (e.g., Figure 6a and Case S8 in Table 3). This is consistent with the high stress (up to ~160 MPa) and high effective viscosity in the top 60 km of the flexed plate (Figures 8c and 8d for cross sections AA' and BB'). Note that the maximum effective viscosity is set to be 10^{27} Pa s in the model, but this should not affect the lithospheric stress relaxation and deformation on the time scales (approximately several million years) of interest here. The results from Case R1 therefore suggest that the standard rheological models lead to a too stiff lithosphere to explain the observed flexure.

[56] As is the case of the S models with an elastic plate thickness of 60 km, there is also a neutral surface with minimum stress and strain rate at a depth of ~30 km below the loads and in their adjacent regions in Case R1 (Figures 8c

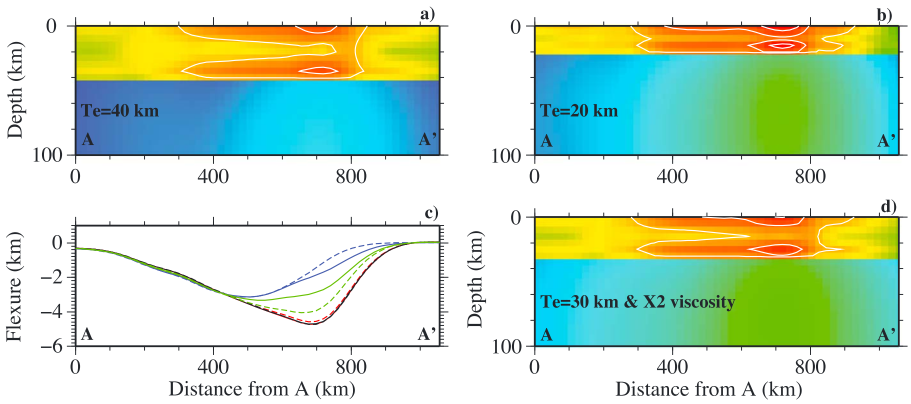

Figure 7. Distribution of the second invariant of stress for the present day for Cases (a) S5 and (b) S2 that have an effective elastic thickness of 40 km and 20 km, respectively, (c) flexures for Cases S1, S8, S9, and S11, and (d) distribution of the second invariant of stress for the present day for Case S9 with elastic thickness of 30 km and 2×10^{21} Pas viscosity for the mantle. All are for cross section AA'. In Figures 7a, 7b, and 7d, the stress contours are for 100, 300, and 500 MPa, and the color scale is given in Figure 5. In Figure 7c, the black, green, and blue curves are for the present day, 480, and 720 Ka before the present day, respectively, while the solid and dashed curves are for Cases S1 and S11, respectively (note that the black dashed and solid curves for the present day are overlapped). The dashed and solid red curves are for the present-day Cases S9 and S10, respectively.

and 8e). The maximum stress of $\sim$160 MPa occurs at a depth of 55 km below Hawaii, while the maximum strain rate of $\sim 10^{-16}\,\mathrm{s}^{-1}$ is at $\sim$65 km depth where the effective viscosity is not as high as at shallower depths, which facilitates stronger deformation. With a frictional coefficient $\mu_f = 0.7$, the frictional strength exceeds the maximum stress even at relatively shallow depths, and consequently does not have significant effects on lithospheric stress and flexure.

[57] *Mei et al.* [2010] reported an uncertainty of ±50 KJ/mol for activation energy E_p. Case R2 uses the lower bound value of E_p, i.e., 270 KJ/mol, and is otherwise identical to Case R1. The reduced E_p weakens the lithosphere and leads to slightly larger flexures and an improved misfit in Case R2 (a misfit of 0.492 in Table 3). Case R3 employs a temperature threshold of 1000°C between the high-temperature creep and low-temperature plasticity regimes but is otherwise identical to Case R1. The larger temperature threshold strengthens the lithosphere slightly, causing the misfit to increase to 0.605 (Table 3).

[58] Cases R4–R7, which use different rheological parameters for the high-temperature flow law, demonstrate that the flexures are mostly insensitive to rheological properties at high temperatures (>800°C). Cases R4 and R5, for example, have an activation energy E_c of 240 KJ/mol and 480 KJ/mol (Table 3), respectively, which differs from Case R1's 360 KJ/mol but otherwise is identical to Case R1. The calculated flexures from these two cases have nearly the same misfit to the observed as in Case R1 (Table 3). In Case R6, the asthenospheric viscosity η_0 is reduced to 10^{19} Pa s, while Case R7 has a reduced transition stress $\sigma_{\mathrm{tran}} = 3 \times 10^4$ Pa (Table 3). Both Cases R6 and R7 assume $E_c = 480$ KJ/mol. Again, these two cases show similarly large misfits for the flexures (Table 3). That the rheological properties at high temperatures do not affect the flexures significantly is expected, because the high-temperature flow law only affects the mantle and lithosphere at depths larger than $\sim$60 km while the loads are mostly supported by the lithosphere at shallower depths. Consequently, in the following calculations we will focus our effort on how low-temperature plasticity and frictional properties of the lithosphere may affect lithospheric deformation.

5.3. Effects of Different Low-Temperature Plastic Flow Laws

[59] Cases R8, R9, and R10 are based on the low-temperature plasticity laws of *Evans and Goetze* [1979], *Raterron et al.* [2004], and *Katayama and Karato* [2008], respectively (Table 2 for rheological equations and parameters). Of these three cases, Case R9 which uses the equation by *Raterron et al.* [2004] produces the weakest lithosphere and hence the largest flexures and the smallest misfit of 0.383 to the observations, while Case R10 which uses the equation of *Katayama and Karato* [2008] produces the largest misfit at 0.459 (Table 3). The flexures from Cases R8, R9, and R10 correspond to those from elastic thickness of 47 km, 43 km, and 51 km, respectively (Table 3). *Katayama and Karato* [2008] also reported uncertainties for Peierls stress and the pre-exponential constant. We therefore recomputed Case R10 with the lower bound lithospheric strength but only found a small decrease of the misfit from 0.459 to 0.439. However, each of the three cases has smaller misfits than Case R1 that assumes the low-temperature plasticity of *Mei et al.* [2010]. This is consistent with the statement of *Mei et al.* [2010] concerning their plastic rheology producing the strongest lithosphere compared with previous studies.

[60] We note that the rheological equations of *Mei et al.* [2010] and *Katayama and Karato* [2008] include the stress in both the exponential function and pre-exponential term, while the stress only appears in the exponential function in *Raterron et al.* [2004] and *Evans and Goetze* [1979] (see Table 2). The latter form may produce a nearly constant, stress-independent strain rate, when the lithospheric stress is $\sim$200 MPa or less as in our loading models, making it difficult to incorporate in loading models. Certainly, it would

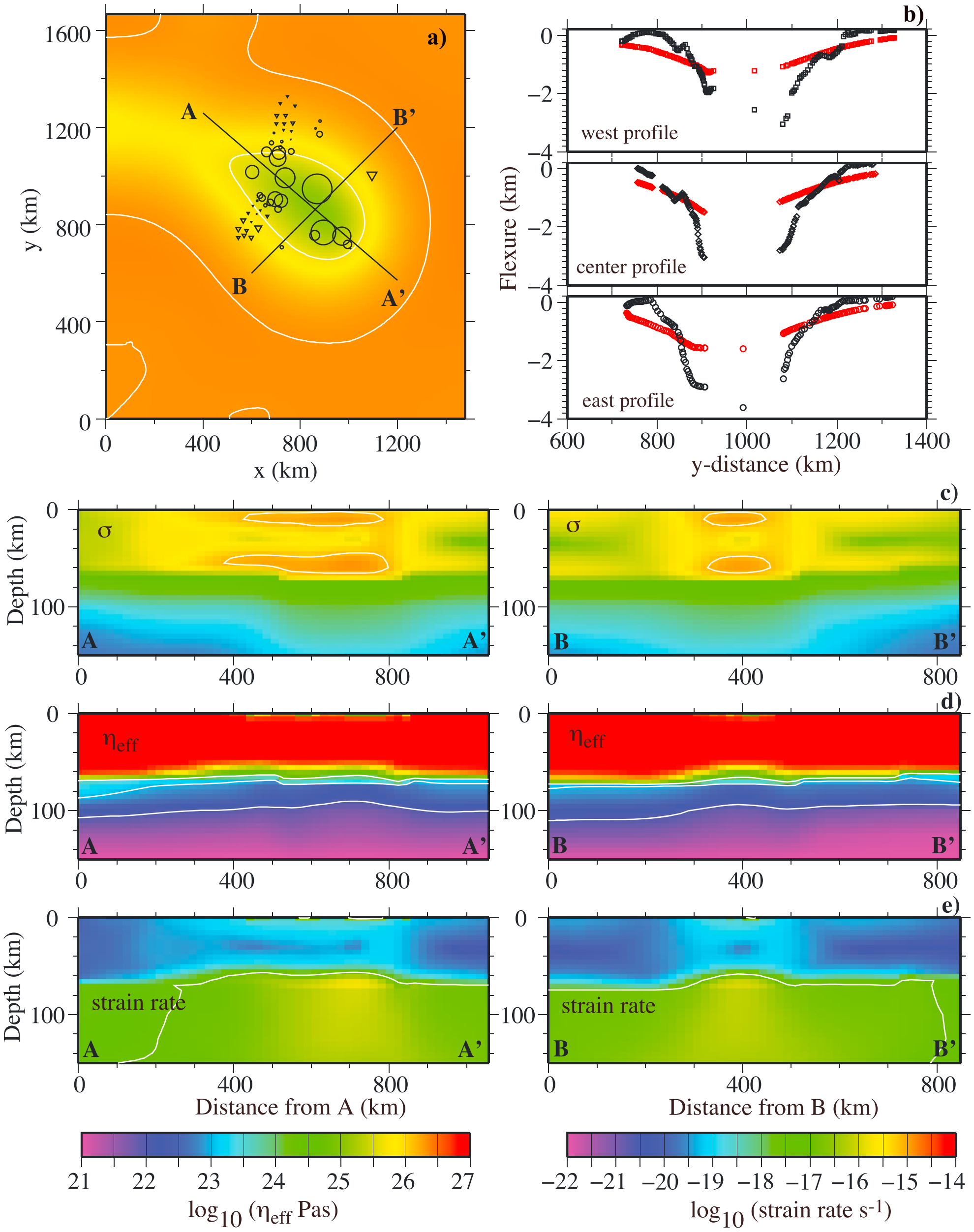

Figure 8. Model results for the present day for Case R1. (a) The present-day flexures in a mapview and (b) for the three profiles that intersect the Hawaiian Islands ridge between Oahu and Molokai (plotted against y coordinates), (c) distribution of the second invariant of stress, (d) effectively viscosity, and (e) strain rate for cross sections AA' and BB'. The color scale for stress is in Figure 4. See Figure 4 caption for the symbols in Figures 8a and 8b. The stress contour in Figure 8c is for 100 MPa; the viscosity contours in Figure 8d are for 10^{22}, 10^{23}, and 10^{24} Pas, respectively; the strain rate contours are for 10^{-17} s^{-1}.

be useful if the experimental data of *Raterron et al.* [2004] and *Evans and Goetze* [1979] could be expressed in a similar way to that of *Mei et al.* [2010]. For our remaining model calculations, we limit our discussion to the low-temperature plasticity equation in *Mei et al.* [2010].

[61] One outstanding question is the form of the low-temperature plasticity law that is required to explain the observed flexures in the vicinity of the Hawaiian Islands. To address this question, we computed Cases R11–R15 in which the low-temperature plasticity of *Mei et al.* [2010] (i.e., equation (11)) was used with the same Peierls stress σ_p and activation energy E_p but a different pre-exponential constant A_t (Table 3). Specifically, A_t is increased by 2, 4, 6, 8, and 10 orders of magnitudes in Cases R11, R12, R13, R14, and R15, respectively, with the strongest lithosphere in Case 11 and the weakest in Case R15. As lithospheric strength decreases, the load-induced flexures increase. However, Case R14 produces the best overall match to the observed flexures (Figures 9a and 9b) with a misfit of 0.295 (Figure 6b and Table 3). Case R15 with the weakest lithosphere overpredicts the flexure, causing a larger misfit compared with Case R14.

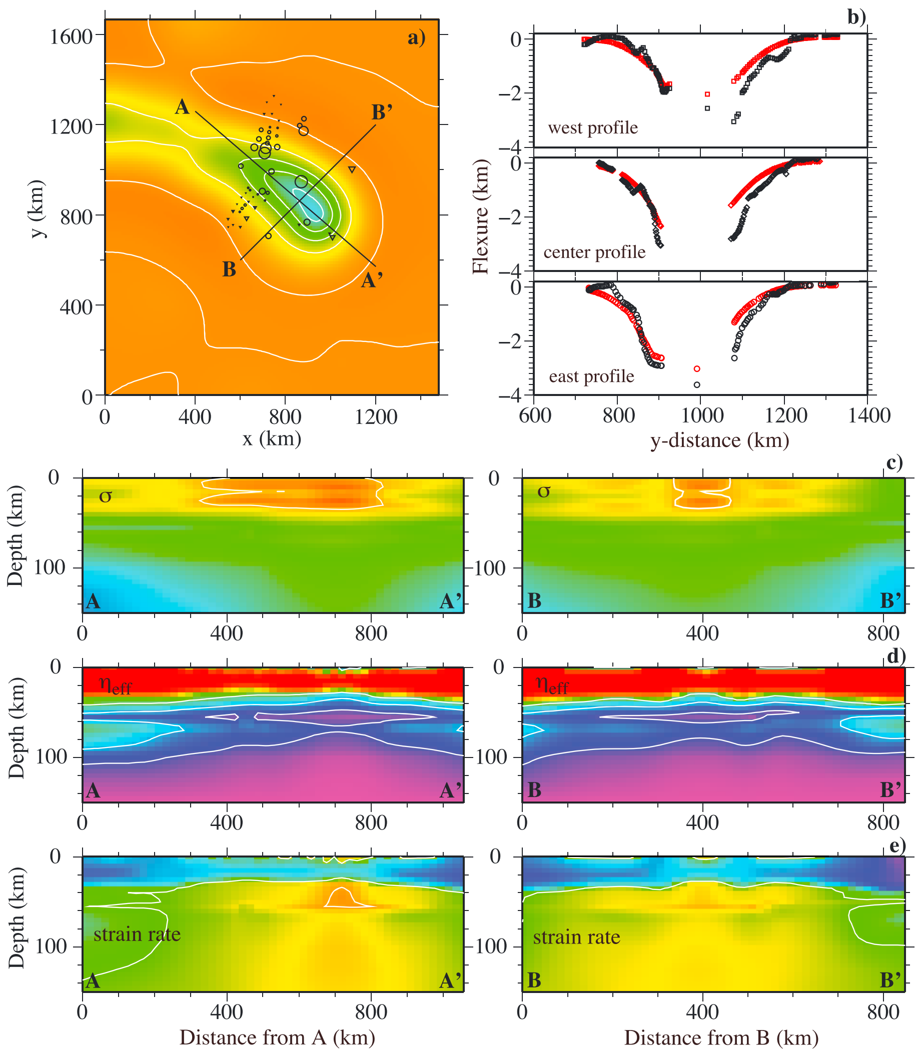

Figure 9. Model results for the present day for Case R14. (a) The present-day flexures in a mapview and (b) for the three profiles that intersect the Hawaiian Islands ridge between Oahu and Molokai (plotted against y coordinates), (c) distribution of the second invariant of stress, (d) effectively viscosity, and (e) strain rate for cross sections AA' and BB'. The color scale for stress is in Figure 4, and the color scales for viscosity and strain rate are in Figure 8. See Figure 4 caption for the symbols in Figures 9a and 9b. The stress contour in Figure 9c is for 100 MPa; the viscosity contours in Figure 9d are for 10^{22}, 10^{23}, and 10^{24} Pas, respectively; the strain rate contours are for 10^{-17} s^{-1} and 10^{-15} s^{-1}.

[62] Compared with Case R1 that uses the reference rheological parameters, Case R14 with reduced lithospheric strength produces a significantly thinner plate at the present day that contains higher stress and strain rate (Figures 8c–8e and 9c–9e). The higher stress in Case R14 leads to a clearly defined increased flexure, which is equivalent to a reduced effective viscosity in high-stress regions below the loads and in the bending regions due to the nonlinear rheology (Figures 9c–9e). The stress pattern from Case R14 is similar to Case S1 with 30 km elastic thickness that has a similarly small misfit to the observed flexures (0.311 in Table 3), although Case S1 is associated with a significantly larger stress (Figure 5b).

[63] It is instructive here to compare the depth dependence of stress and strain rate in the Hawaiian Island region for Cases S1, R1, and R14 with the distribution of seismicity (e.g., Figure 3c) [*Anchieta et al.*, 2011]. The averaged stress and strain rate for the present day is computed over a region that is centered at Hawaii with a radius of 250 km for these models (Figures 10a–10d). Case S1 shows two stress peaks at the surface and 25 km depth, respectively, and a stress minimum at 15 km depth, while Case R1 has two stress peaks at depths of 10 km and 60 km, respectively, and a stress minimum at ~30 km depth (Figure 10a). That the stress increases from the surface to 10 km for Case R1 reflects the increased frictional strength with depth for this case. The magnitude of strain rates is generally proportional to the stress, except for the mantle where the relatively small viscosity may lead to a large strain rate even with small stress (Figure 10b). The averaged stress and strain rate for Case R14 (Figures 10c–10d) shows similar patterns to Case R1, but the stress and strain rate minima and the second stress peak for Case R14 occur at much shallower depths than in Case R1.

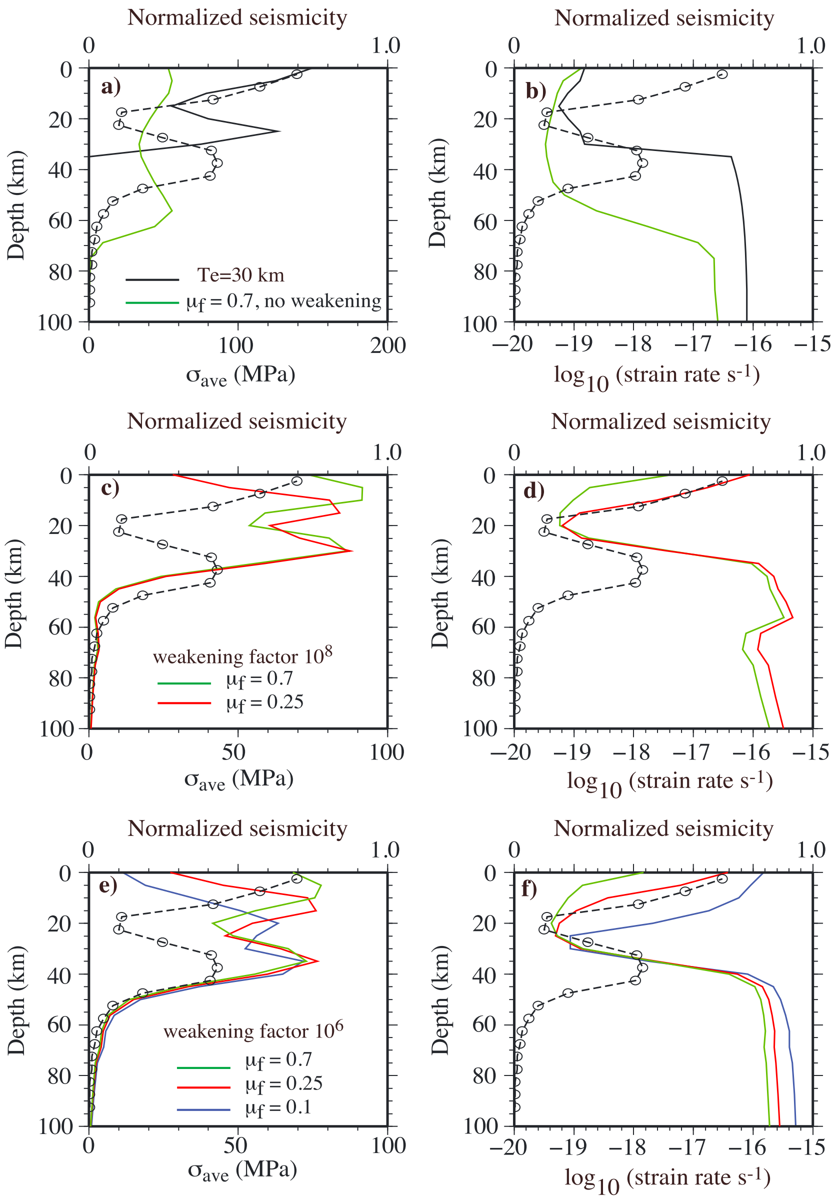

Figure 10. Depth dependences of horizontally averaged second invariant of stress and strain rate for (a, b) Cases S1 and R1, (c, d) Cases R14 and R23, and (e, f) Cases R13, R22, and R20. Also shown in Figures 10a–10f is the depth distribution of normalized seismicity (dashed curves with circles) at Hawaii [*Anchieta et al.*, 2011] (also see Figure 3c). The average is done within a circle of 250 km radius centered at the big island of Hawaii.

[64] Interpretation of the seismicity distribution in terms of our stress and strain rate calculations is not straightforward. However, the seismicity in the Hawaiian Islands region shows a remarkably similar depth dependence to the modeled stress and strain rate. If we take the view that the high (low) level of seismicity corresponds to large (small) stress or strain rate in the lithosphere, we may conclude that the depth-dependent stress and strain rate for Case R14 with weakened lithosphere matches well with the seismicity pattern (Figures 10c–10d), but the seismicity minima at ~20 km depth and the second seismicity peak at ~40 km depth are at too large depths for Case S1 but at too small depths for Case R1 (Figures 10a–10b). Cases R1, R11–R15 therefore demonstrate that the lithosphere needs to be significantly weaker than predicted by the low-temperature plasticity law of *Mei et al.* [2010] in order to match the observed flexures and distribution of seismicity in the Hawaiian Island region.

[65] Although we have already discussed the effects of loading history (e.g., the shortened loading times) and stress relaxation in Cases S9–S11, we need to revisit these issues for the R models, which incorporate more realistic thermal and rheological structures. For example, lithospheric viscosity in the R models varies continuously with temperature and hence depth and so we would expect a more continuous lithospheric stress relaxation with time. This potentially makes both the lithospheric thermal structure and loading times more critical to the model results. We have employed version 1.6 seafloor age [*Muller et al.*, 1997] for determining

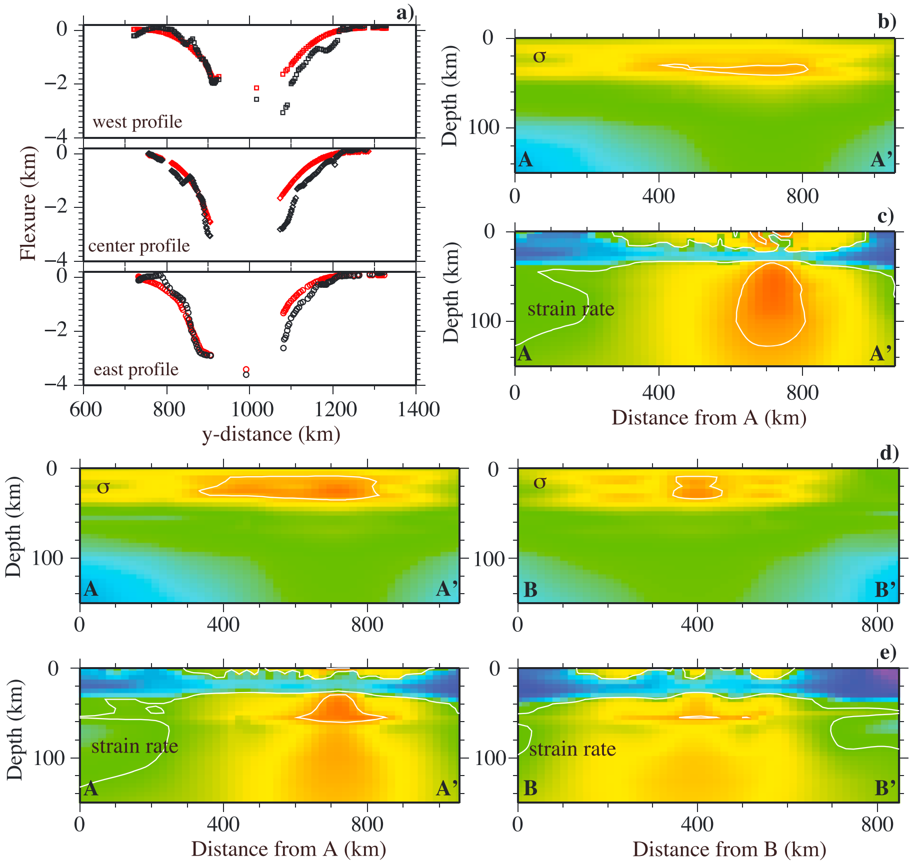

Figure 11. (a) The present-day flexures for the three profiles that intersect the Hawaiian Islands ridge between Oahu and Molokai (plotted against *y* coordinates), (b, c) distribution of the second invariant of stress and strain rate for cross section AA' for Case R20, and (d, e) distribution of the second invariant of stress and strain rate for cross sections AA' and BB' for Case R23. The color scales for stress and strain rate are in Figures 4 and 8, respectively. See Figure 4 caption for the symbols in Figure 11a. The stress contour in Figure 9c is for 100 MPa, and the strain rate contours are for 10^{-17} s^{-1} and 10^{-15} s^{-1}.

lithospheric thermal and viscosity structures for Cases R1–R15 and for correcting the effect of thermal isostasy on the observed topography and flexures. In Case R16, we repeated Case R14 using the updated, high-resolution, oceanic crustal age model of version 3.2 [*Muller et al.*, 2008] for computing lithospheric thermal and viscosity structures and for correcting the topography and flexures. We found that the model misfit was slightly reduced from 0.295 for Case R14 to 0.291 for Case R16, suggesting that the effect of the crustal age difference between versions 1.6 and 3.2 on our model results is minor. In Case R17, we doubled the loading times for each of the loading stages listed in Table 1, but Case R17 is otherwise identical to Case R14. This time adjustment makes the loading times for Oahu and Molokai more consistent with the observations based on rock outcrop data [*Clague and Dalrymple*, 1988]. However, we found that the adjusted times in Case R17 have only a small effect on the model results of the present-day flexures which yield a misfit of 0.291, compared with 0.295 for Case R14 (Table 3). It should be pointed out that Case R17 with a doubled loading time can also be realized approximately by rescaling Case R14 using a doubled η_0 or 2×10^{20} Pa s, as discussed in section 5.1. However, in contrast to the two-layer S models in section 5.1, the results from Case R17 differ slightly from simply rescaling Case R14 because of the imposed viscosity cutoff at $10\eta_0$ for computational efficiency.

5.4. Effects of Reduced Frictional Coefficient

[66] In Cases R1–17 presented in preceding subsections, the frictional coefficient μ_f is 0.7. It has been suggested that pore pressure may lead to reduced frictional strength for the lithosphere [e.g., *Kohlstedt et al.*, 1995]. This effect may be modeled by reducing μ_f. Reducing μ_f may be equivalent to weakening lithosphere from the top, in contrast to Cases R11–R17 that reduce lithospheric strength from the bottom by reducing the pre-exponential factor of the low-temperature plasticity law. Six cases with varying weakening factor and μ_f are computed to examine the effect of reducing μ_f (Cases R18–R23 in Table 3). Even with μ_f reduced to 0.1, significant weakening for the low-temperature plasticity case of *Mei et al.* [2010] is needed in order to match the observed flexures (Figure 6b). For example, Case R18 with no weakening is identical to Case R1, except that μ_f is reduced from 0.7 to 0.1. The misfit to the flexures for Case R18 is as high as 0.472 (Table 3). With μ_f= 0.1, Cases R19 and R20 with a weakening factor of 10^4 and 10^6 have a misfit of 0.336 and 0.278, respectively (Figure 6b, Table 3), and the latter is the smallest misfit for all the cases computed in this study

(Figure 11a). Case R23 with a weakening factor of 10^8 and $\mu_f = 0.25$ only reduces the misfit slightly, compared with Case R14 that has $\mu_f = 0.7$ but is otherwise identical to Case R23 (Figure 6b).

[67] Reducing μ_f leads to a reduced lithospheric strength, more deformation, and smaller stress at shallow depths. This is evident by comparing the depth distributions of stress and strain rate of Case R23 (Figures 11d and 11e) with Case R14 (Figures 9c and 9e). Case R23 with $\mu_f = 0.25$ shows significant deformation down to ~15 km depth below the loads and in the bending zones, while the deformation is limited to a much shallower depth in Case R14 with $\mu_f = 0.7$. Case R20 with $\mu_f = 0.1$ displays significant deformation down to an even larger depth of ~20 km, while the stress at shallow depths is greatly reduced (Figures 11b and 11c). The horizontally averaged stress and strain rate for cases with a different weakening factor and μ_f demonstrate the depth dependences more clearly (Figures 10c–10f). First, the stress increases with depth more slowly for a smaller μ_f, as expected from Byerlee's law, leading to a deeper location for the first stress peak for a smaller μ_f. Second, the second stress peak appears to occur at the same depth of 30–40 km, independent of μ_f. Third, the minimum strain rate occurs approximately at the same depth location as the stress minimum, i.e., at a larger depth for a smaller μ_f.

[68] It is interesting to compare the depth dependences of averaged stress and strain rate from the models with the observed seismicity. Among the cases with a relatively small misfit between observed and calculated flexures (i.e., ~0.30 or less for Cases R14, R20, R22, and R23 in Table 3 and Figure 6b), all the cases with $\mu_f = 0.7$ and 0.25 yield a minimum strain rate at ~20 km depth which is the same depth where the seismicity is a minimum (Figures 10d and 10f), but Case R20 with $\mu_f = 0.1$ has the minimum strain rate and stress at ~30 km depth, which is significantly deeper. All these cases produce a peak in strain rate near the surface, which corresponds well to the peak in seismicity. These cases also produce a stress peak at ~30–40 km, which corresponds well with the second peak in seismicity (Figures 10c and 10e). These model calculations suggest that the observed flexures and seismicity at Hawaii are best explained by a lithospheric rheology with that combines a frictional coefficient μ_f between 0.25 and 0.7 with a low-temperature plasticity law that is significantly weaker than *Mei et al.* [2010] by a factor of 10^6 and 10^8.

6. Discussion

6.1. Low-Temperature Plasticity for Lithosphere

[69] Lithosphere deformation may operate under three regimes: frictional sliding, semi-brittle, and plastic flow (i.e., low-temperature plasticity and high-temperature creep), and all three regimes are highly nonlinear. By modeling the nonlinear deformation of the lithosphere in response to the volcanic loads of the Hawaiian Islands and comparing them to the seismically constrained crustal flexures, stress and strain rate, we have shown that the lithospheric deformation at ~1 Ma time scales is only sensitive to frictional sliding and low-temperature plasticity and that the lithosphere is significantly weaker than predicted from laboratory studies on mantle rock or mineral samples. In particular, we have found that the pre-exponential factor in the rheological equation of low-temperature plasticity of *Mei et al.* [2010] needs to be reduced by 6 to 8 orders of magnitude, in order to match the observations (Figure 6b). Our calculations show that low-temperature plasticity from other laboratory studies [*Evans and Goetze*, 1979; *Raterron et al*., 2004; *Katayama and Karato*, 2008] also leads to too strong lithosphere to explain the flexures that are observed.

[70] There is likely to be a significant uncertainty exactly where the brittle-plastic transition (i.e., the transition from the semi-brittle deformation to low-temperature plasticity or BPT) occurs (Figure 1) [*Kohlstedt and Mackwell*, 2009; *Mei et al*., 2010], and it is important to examine its effect on our model results. As discussed in section 3.1.2, with the poorly understood semi-brittle regime, which is unaccounted for in our models, the effective lithospheric viscosity for temperatures colder than 800°C is mostly determined from the low-temperature plasticity, except possibly for shallow regions of lithosphere where the frictional strength is predicted to be small from Byerlee's law. With this model assumption, it is likely that the semi-brittle deformation in some regions of the lithosphere is approximated by low-temperature plastic deformation. However, we believe that this approximation is justified and may not introduce significant errors. This is because the semi-brittle deformation may only be important in the lithosphere at temperatures ~400–500°C (i.e., BPT) where the lithospheric strength and effective viscosity are high (Figure 1) and where the lithospheric stress is not relaxed and is supported elastically on long loading time scale (i.e., several million years) (i.e., it behaves essentially elastically). On such time scales, the effective viscosity only needs to be as high as ~10^{24}–10^{25} Pa s for the lithosphere to behave elastically. Our model calculations show that the effective viscosity predicted from low-temperature plasticity is sufficiently high under these temperatures and stress conditions (Figure 9). Therefore, we do not believe that representing the semi-brittle regime by low-temperature plasticity introduces significant errors to our results.

[71] In appealing to the low-temperature plasticity to explain the seismically constrained observations, we only varied the pre-exponential factor in the rheological equation for low-temperature plasticity while keeping the activation energy, Peierls stress, and other parameters the same as that in *Mei et al.* [2010]. However, this does not rule out other possible ways to weaken the lithosphere, such as reducing activation energy or Peierls stress. As pointed out by *Mei et al.* [2010], there are significant differences among the published low-temperature plasticity flow laws, due to differences in experimental techniques and conditions. The low-temperature plasticity laws of *Raterron et al.* [2004] and *Demouchy et al.* [2013], for example, lead to relatively weak lithosphere, while those of *Mei et al.* [2010] represent the strongest. We did not fully test how much variation in these flow laws would be required in order to match the observations. As discussed in section 5.3, *Raterron et al.* [2004] and *Evans and Goetze* [1979] employed a purely exponential flow law that is not as useful in modeling lithospheric deformation with $<$100–200 MPa stress. The experimental data from these studies may be refit to the same equations as *Mei et al.* [2010] that can be fully tested with our loading models in future studies. It is also important to note that when applying flow laws derived from laboratory studies to model in situ

observations (e.g., flexures), although it is often necessary to vary one or more parameters (e.g., activation energy or pre-exponential factor) from modeling perspective, the resulting flow laws may become inconsistent with the original experimental data.

[72] Laboratory studies for low-temperature plasticity are often performed on single-crystal or polycrystalline samples at significantly larger strain rate (~$10^{-5}\,\mathrm{s}^{-1}$) and stress (~1000 MPa) conditions than in natural settings. While these laboratory studies provide important insights about the physics of deformation, a long-standing challenge has been how to apply these studies to in situ geodynamic and tectonic problems on the one hand and whether other mechanisms contribute to the deformation on the other hand. For example, *Ohuchi et al.* [2010] reported that the presence of orthopyroxene may reduce lithospheric strength significantly. Based on analyses of peridotite mylonites, *Warren and Hirth* [2006] and *Jaroslow et al.* [1996] suggested that grain size reduction may lead to shear localization and permit diffusion creep at temperatures down to ~600°C, thus weakening oceanic lithosphere significantly. We believe that modeling in situ observations such as load-induced flexure is essential for developing independent and complementary constraints on lithospheric rheology and for calibrating laboratory studies. Our conclusion for relatively weak lithosphere is consistent with previous loading calculations using linear viscoelastic rheology, which indicated that in order to explain the relationship between elastic plate thickness and plate and load age, the activation energy for the mantle rheology was required to be small at ~150 KJ/mol [*Courtney and Beaumont*, 1983; *Watts and Zhong*, 2000; *Watts et al.*, 2013]. However, due to technical limitations, these previous loading calculations only considered diffusion creep and excluded the nonlinear deformation regimes.

6.2. Coefficient of Friction of the Lithosphere

[73] Lithospheric strength at relatively shallow depths is limited by the frictional properties of the lithosphere (i.e., Byerlee's law), and enhanced pore pressures may reduce frictional and hence lithospheric strength [e.g., *Kohlstedt et al.*, 1995]. The effect of enhanced pore pressures may be simulated by reducing the frictional coefficient, μ_f. In our loading calculations, reducing μ_f results in a weakened lithosphere, reduced stress, and enhanced deformation at shallow depths (<20 km) (Figures 11b–11e), which leads to increased load-induced flexures and an improvement in model misfit (Figure 6b). Depending on the low-temperature plasticity law (i.e., weakening factors of 10^6 or 10^8), loading models with μ_f from 0.7 to 0.1 explain the observed flexures nearly equally well (Figure 6b), suggesting a trade-off between low-temperature plasticity and μ_f.

[74] However, the depth distribution of seismicity beneath Hawaii may provide constraints on μ_f, if seismicity can be regarded as a measure of the regional deformation [e.g., *England and Molnar*, 1997] rather than a local response to magmatic processes. *Anchieta et al.* [2011] showed that seismicity is at a minimum at a depth of ~20 km in Hawaiian Islands region (Figure 3c). Among the models that match well the observed flexures with weakening factor of 10^6–10^8 and μ_f from 0.1 to 0.7 (Figure 6b), all the models with μ_f from 0.25 to 0.7 produce a minimum in stress and strain rate at about the same depth (i.e., ~20 km) as the observed minimum in seismicity, but the model with $\mu_f = 0.1$ yields a minimum in stress and strain rate at a significantly larger depth (~30 km) (Figures 10c–10f). Although this model with $\mu_f = 0.1$ matches the seismically constrained flexures the best (Case R20 in Table 3 and Figure 6b), the distribution of seismicity appears to support μ_f between 0.25 and 0.7. Our loading models also indicate that averaged strain rate and spatially varying strain rate at shallow depths are very sensitive to μ_f (Figures 10d, 10f, 11c, and 11e). An additional constraint on μ_f may be possible by further analysis of the seismicity distribution and comparison with the modeled strain rates.

[75] In situ stress measurements in deep (up to 9 km depth) boreholes on continents indicate that μ_f is 0.6 which is consistent with the results of laboratory studies [*Zoback and Townend*, 2001]. If we consider the effect of hydrostatic pore-fluid pressure, then the nominal μ_f is ~0.4. Our study, if we take into account the seismicity constraints, suggests that μ_f ranges from 0.25 to 0.7 for oceanic lithosphere, which is broadly consistent with the in situ stress measurements on continents. Our calculations show that the load-induced lithospheric stress at Hawaii may reach 100–200 MPa (Figures 9c, 11b, and 11d) which is in accord with previous studies [e.g., *Kanamori*, 1980]. This stress may reflect the highest lithospheric stress, given that Hawaiian Islands are among the largest loads to have been emplaced on the surface of the Earth.

[76] It should be pointed out that interpreting the short-term seismic deformation in the context of long-term lithospheric deformation is not without difficulties. It has been suggested on the basis of frictional behavior of olivine aggregates, for example, that the depth of the ~600°C isotherm is the approximate limit of the seismicity in the oceanic lithosphere and hence marks the BPT [*Boettcher et al.*, 2007]. However, at Hawaii, the 600°C isotherm is at ~40 km depth [e.g., *Watts and Zhong*, 2000] where the seismicity is at its second peak with notable seismicity that goes beyond 60 km depth (Figure 3b) [*Anchieta et al.*, 2011]. This suggests that the brittle/seismic deformation and plastic flow regimes may overlap and so we cannot rule out either regime at a depth >40 km. Our calculations demonstrate that the oceanic lithosphere at Hawaii at a depth >40 km must have sufficiently small effective viscosity beneath the loads such that it is unable to support the stress on a ~1 Ma loading time scale.

6.3. Implications for Mantle Dynamics and Plate Tectonics

[77] One of the most important goals in geodynamics is to understand how plate tectonics emerges dynamically from mantle convection. In particular, we may ask why Earth has plate tectonics or mobile lid convection while other terrestrial planets like Venus have stagnant lid convection [*Bercovici*, 2003]. Treating the mantle as purely viscous flow with pseudoplastic rheology, *Moresi and Solomatov* [1998] reported that mobile lid convection is expected if the coefficient of friction μ_f is between 0.03 and 0.13, while larger μ_f leads to stagnant lid convection. Similar conclusions have been drawn from 3-D convection models [*Tackley*, 2000; *Foley and Becker*, 2009; *van Heck and Tackley*, 2008]. Some model calculations employed a constant yield stress and found that the yield stress needs to be $< \sim 100$ MPa to produce mobile lid convection [*Richards et al.*, 2001].

[78] Our loading calculations show that while the seismically constrained flexures in the region of the Hawaiian Islands permit a coefficient of friction μ_f from 0.1 to 0.7 for oceanic lithosphere, the depth-dependent seismicity at Hawaii is consistent with μ_f ranging from 0.25 to 0.7 but not 0.1. Therefore, our results present a challenge to those mantle dynamic models that consider a small coefficient of friction in order to generate a mobile lid, plate tectonic type of mantle convection. On the other hand, the fact that our loading studies reveal that the maximum lithospheric stress is 100–200 MPa is collaborative evidence to support those mantle dynamic models that consider relatively small (~100 MPa) yield stresses. However, it is also important to recognize that the maximum lithospheric stress that we have derived does not necessarily reflect the lithospheric strength. We believe that the loading calculations as presented here help constrain lithospheric rheology and stress that should ultimately improve our understanding of the conditions that are required for the generation of plate tectonics on Earth.

6.4. Limitations of Our Loading Models and Future Improvements

[79] Our loading models ignore mantle compressibility and exclude the crust. Mantle compressibility and the crust do not, in general, affect the load-induced vertical motion significantly, as demonstrated in postglacial rebound studies [*Paulson et al.*, 2007]. Therefore, we believe that our general results are not affected significantly by ignoring these factors. We note though that the differential restoring force at the top and bottom of the oceanic crust is included in our models. Mantle compressibility and the crust have been recently incorporated in a spherical version of our loading models (i.e., in the code CitcomSVE) [*A et al.*, 2013]. A significant advantage of including mantle compressibility is to more realistically simulate mantle elastic structure (e.g., from either preliminary reference Earth model or regional seismic models). We plan to implement mantle compressibility and the crust into our 3-D regional loading models as in CitcomSVE [*A et al.*, 2013] to make the model more generally applicable to geophysical problems.

[80] The loading models presented here are based only on surface loads and ignore the possibility of subsurface (i.e., buried) loads, as is the case in most previous oceanic flexure studies [e.g., *Watts and ten Brink*, 1989; *Wessel*, 1993; *Pritchard et al.*, 2007]. Buried loads include intrusive volcanic rocks often found near the Moho which may have a larger density (~3000 kg/m^3) than the basaltic/gabbroic crust (~2800 kg/m^3) [e.g., *Contreras-Reyes et al.*, 2010; *Richards et al.*, 2013]. It is challenging to assess the role of buried loads and their effects. However, we note that previous elastic plate models without buried loads reproduced the observed free air anomalies remarkably well at submarine volcanic loads [e.g., *Watts and ten Brink*, 1989; *Wessel*, 1993], suggesting that buried loads may not affect the loading calculations significantly. Clearly, this is a topic that deserves more future work.

[81] The predicted flexures from our loading models do not match the seismically constrained flexures north of Oahu/Molokai as well as they do for other comparison sites. *Watts and ten Brink* [1989] encountered a similar problem in their elastic plate modeling. We computed models to replace an infill dominated by volcanoclastic sediments (i.e., density of 2300 kg/m^3) with one comprised mainly of volcanic rocks (i.e., density of 2800 kg/m^3) but found the differences to be small. *Watts and ten Brink* [1989] suggested that the Molokai Fracture Zone, which extends across the Pacific Ocean from a transform fault on the East Pacific Rise, to east of Molokai and then reappears on the west of the Hawaiian Islands in the Mid-Pacific mountains region (Figure 2b), may have affected the preexisting topography prior to the main island shield building phase in the region. For example, the crust near the fracture zone northeast of the channel separating Oahu and Molokai is thinner than beneath the Hawaiian moat and flanking arch [*Watts and ten Brink*, 1989]. We corrected the crustal thickness effects on flexures assuming local isostatic compensation (equation (17)), but this may introduce some errors in the flexures. Future work is needed to resolve this discrepancy better.

[82] We used simplified loading histories (Table 1) and demonstrated that loading histories do not significantly affect the present-day flexure, based on comparison between Cases S1 and S11. However, loading histories do influence the vertical motion history (Figure 3b) and may affect present-day strain rates as well. Future studies may explore the possibility to use observed vertical motion history and strain rates at Hawaii as discussed here to constrain both lithospheric rheology and loading histories.

[83] Finally, several other deformation and weakening mechanisms relevant to the lithosphere may need to be further investigated. First, while *Wessel* [1993] and *Watts and ten Brink* [1989] considered the potential effect of the Molokai Fracture Zone as a fault in their elastic plate model, our models ignore any possible weakening of the lithosphere in the vicinity of the fracture zone. However, seismicity at Hawaii does not show any preferred orientation with the trend of the Molokai Fracture Zone [*Anchieta et al.*, 2011]. This suggests to us that the fracture zone may not have significantly different long-term strength from the normal oceanic lithosphere, thus supporting our models. Indeed, elastic thickness estimates at nonslipping fracture zones suggest that they may actually be stronger than normal oceanic lithosphere [*Wessel and Haxby*, 1990]. Second, the effects of orthopyroxene [*Ohuchi et al.*, 2010], shear localization from grain size reduction [*Warren and Hirth*, 2006], and the role of the poorly understood semi-brittle mechanism need to be examined in future studies.

7. Conclusions

[84] We have developed a 3-D finite element model for computing the load-induced surface deformation and stress field for lithosphere and mantle with a nonlinear viscoelastic rheology. The new loading model has been applied to a lithosphere with a realistic nonlinear rheology which includes frictional sliding (i.e., Byerlee's law), low-temperature plasticity, and high-temperature creep and used to determine the flexures and stresses associated with the emplacement of the volcanic load of the Hawaiian Islands on ~80 Ma Pacific Ocean lithosphere for the last few million years. By comparing model predictions with the seismically constrained flexure of Pacific oceanic crust and the depth dependence of seismicity in the Hawaiian region, we have sought to place new constraints on the rheology of oceanic lithosphere. Our main results are summarized as follows.

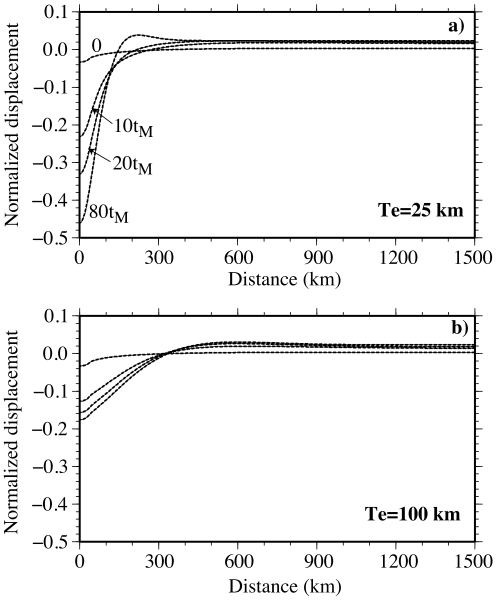

Figure A1. Normalized flexures versus distance from the center of the load for 3-D benchmark cases with elastic plate thickness of (a) 25 km and (b) 100 km. Both analytical (dashed curves) and finite element (solid curves) solutions are plotted, but they nearly overlap each other. The four curves in each figure are for times of 0, $10t_M$ (9512.95 years), $20t_M$ (19,025.9 years), and $80t_M$ (76,103.6 years) since the loading. Note that the load does not vary in y direction and that the profile from 3-D model is taken at $y = 300$ km (i.e., at the middle of the box).

[85] 1. The flexure of oceanic lithosphere caused by volcano loads can be modeled using a viscoelastic model; a special case of which is the classical elastic plate model. In accord with previous studies, our 3-D viscoelastic loading models show that the elastic plate beneath the Hawaiian Islands needs to be ~30 km thick in order to fit the seismically constrained flexures.

[86] 2. Flexure at the Hawaiian Islands is controlled by low-temperature plasticity and frictional sliding but are insensitive to high-temperature (>800°C) creep. Hence, observations of flexures only provide constraints on low-temperature plasticity and frictional sliding rheology.

[87] 3. Laboratory-derived low-temperature plasticity flow laws tend to predict too thick or too strong lithosphere to match the observed flexures at Hawaii. For example, the recently published low-temperature plasticity flow law of *Mei et al.* [2010] appears too strong and results in a ~60 km thick effective elastic plate for the Hawaiian Islands region. To match the observed flexures, the pre-exponential factor for the low-temperature plasticity flow law of *Mei et al.* [2010] needs to be reduced up to 6 to 8 orders of magnitude.

[88] 4. The observed flexures can be explained by a frictional coefficient μ_f in the range 0.1 to 0.7 with a weakening factor of 6 to 8 orders of magnitude for low-temperature plasticity. However, $\mu_f = 0.1$ weakens the shallow part of the lithosphere so much that it causes the minima in strain rate and stress to occur at too large depths to be consistent with the depth distribution of seismicity in the Hawaiian Islands region. Our results therefore suggest μ_f in the range of 0.25 to 0.7, broadly consistent with the laboratory value and in situ borehole measurements in continents.

[89] 5. The maximum lithospheric stress beneath the Hawaiian Island volcanic loads is about 100–200 MPa for models with the realistic nonlinear rheology that fits the observed flexures. Given that Hawaiian Islands are among the largest concentrated loads on Earth, this stress may be viewed as the largest stress in the lithosphere on Earth.

Appendix A: The 2-D and 3-D Benchmark Calculations for Load-Induced Deformation

[90] We present here 2-D and 3-D benchmark calculations to demonstrate the accuracy of our finite element code. For the 2-D Cartesian calculations, the box is 1500 km wide and 600 km deep. The material in the box has a density of 3330 kg m^{-3}, a shear modulus of 3.3333×10^{10} Pa, and a viscosity of 10^{21} Pa s except for a top high-viscosity layer where the viscosity is 10^{26} Pa s. We perform two calculations with different thicknesses for the top layer, one at 25 km and the other at 100 km. A load is applied at the left corner of the surface (i.e., $x = 0$) at time zero and is maintained through time (i.e., a Heaviside function). The load is 40 km wide at the base, 30 km wide at the top, and 1 m high with the same density as the medium below (Figure A1). No infill is considered in these benchmark calculations.

[91] The physics of this type of loading problem is relatively straightforward as described in *Zhong* [1997] and *Watts and Zhong* [2000]. At time zero, the load generates elastic stress in the entire domain that supports the load. With time, the stress in the bottom layer with smaller viscosity relaxes viscously, while the stress in the top layer increases to support the load. The stress in the bottom layer largely vanishes after some characteristic time (i.e., some multiples of the Maxwell time t_M defined as the ratio of the bottom layer viscosity or 10^{21} Pa s to shear modulus). The flexure is relatively small at $t = 0$, as the load is supported by the entire domain. As the stress decreases (increases) in the bottom (top) layer with time, the flexure also increases. After sufficiently long time, the flexure approaches the predictions of the elastic plate model [*Zhong*, 1997].

[92] These two 2-D cases with different top layer thicknesses are computed with both an analytical solution approach [*Zhong*, 1997] and our finite element method. Figure A1 shows the analytical solutions (dashed curves) for the load-induced flexure at time 0, 9512.95, 19,025.9, and 76,103.6 years, or 0, 10, 20, and $80t_M$ where t_M is the Maxwell time defined by the bottom layer viscosity. The case

Table A1. Relative Errors ε in Percentage for the Benchmark Calculations

Case[a]	0[b]	$10t_M$	$20t_M$	$40t_M$	$80t_M$
2-D 25 km	0.70	1.3	0.92	0.69	0.68
2-D 100 km	0.90	1.2	0.88	0.58	0.50
3-D 25 km-m	3.0	0.40	0.20	0.29	0.42
3-D 25 km-p	3.5	0.40	0.18	0.30	0.46
3-D 100 km-m	2.0	0.36	0.32	0.30	0.30
3-D 100 km-m-y	2.4	0.31	0.33	0.30	0.30

[a] Cases 25 km and 100 km are for the thickness of the top layer. For 3-D cases, "-m" designates a profile along the middle of the box at $y = 300$ km, "-p" is for a profile at $y = 600$ km (i.e., the sidewall), and "-y" is for a case with the load that is applied along y direction.

[b] At different time $t = 0$, $10t_M$, $20t_M$, $40t_M$, and $80t_M$, corresponding to 0, 9512.95, 19,025.9, 38,051.8, and 76,103.6 years, respectively.

with 25 km thick top layer shows a larger flexure including the depression and the bulge than that with 100 km thick top layer. For the modeling, 192 and 48 elements are used in horizontal and vertical directions, respectively, with some mesh refinements near the load. Time step Δt is $0.25t_M$. The solutions from the finite element code agree well with analytical solutions with errors that are generally about 1% or less at different times (Table A1), where the errors ε are defined as

$$\varepsilon = \sqrt{\int_0^L [S_{\mathrm{FE}}(x) - S_{\mathrm{ANA}}(x)]^2 \mathrm{d}x} \Bigg/ \sqrt{\int_0^L [S_{\mathrm{ANA}}(x)]^2 \mathrm{d}x}, \qquad \text{(A1)}$$

where S_{FE} and S_{ANA} are the flexures at a given time from finite element and analytical methods, respectively, and $L = 1500$ km is the length of the profile.

[93] These two cases are also computed using the 3-D finite element code for a box that has dimensions of 1500 km, 600 km, and 600 km in x, y, and z directions, respectively, that use 192, 48, and 48 elements in the three corresponding directions. The same load is along the x direction with no variations in the y direction. Mesh refinements are applied in the x-z plane in the same way as in 2-D calculations, but uniform mesh is used in the y direction. Time step Δt is also equal to $0.25t_M$. Flexures as a function of x along a profile at $y = 300$ km (i.e., at the middle of the box) are plotted in Figure A1 (solid curves) at time 0, 9512.95, 19,025.9, and 76,103.6 years for these two cases, showing excellent agreement with the analytical solutions with similarly small relative errors to those from 2-D finite element calculations, except for the elastic response at $t = 0$ for which the errors are ~3% (Table A1). The relative errors for profiles at $y = 0$ and 600 km are also similar (Table A1). The 3-D calculations are also performed with the load applied along the y direction, and the accuracy of the solutions is similar to that with the load applied in the x direction (Table A1). Based on these benchmark calculations, we conclude that our finite element code is sufficiently accurate for the volcano-loading situations discussed in this paper.

[94] **Acknowledgments.** We thank Greg Hirth, an anonymous reviewer, and the Associate Editor for their constructive and careful reviews, and NSF (US-NSF 1114168) and NERC (NE/1026839/1) for their financial support.

References

A, G., J. Wahr, and S. J. Zhong (2013), Computations of the viscoelastic response of a 3-D compressible Earth to surface loading: An application to Glacial Isostatic Adjustment in Antarctica and Canada, *Geophys. J. Int.*, *192*, 557–572, doi:10.1093/gji/ggs030.

Anchieta, M. C., C. J. Wolfe, G. L. Pavlis, F. L. Vernon, J. A. Eakins, S. C. Solomon, G. Laske, and J. A. Collins (2011), Seismicity around the Hawaiian Islands recorded by the PLUME seismometer networks: Insight into faulting near Maui, Molokai, and Oahu, *Bull. Seismol. Soc. Am.*, *101*, 1742–1758, doi:10.1785/0120100271.

Asaadi, N., N. M. Ribe, and F. Sobouti (2011), Inferring nonlinear mantle rheology from the shape of the Hawaiian swell, *Nature*, *473*, 501–504, doi:10.1038/nature09993.

Bercovici, D. (2003), The generation of plate tectonics from mantle convection, *Earth Planet. Sci. Lett.*, *205*, 107–121.

Billen, M. I., and M. Gurnis (2005), Constraints on subducting plate strength within the Kermadec trench, *J. Geophys. Res.*, *110*, B05407, doi:10.1029/2004JB003308.

Boettcher, M. S., G. Hirth, and B. Evans (2007), Olivine friction at the base of oceanic seismogenic zones, *J. Geophys. Res.*, *112*, B01205, doi:10.1029/2006JB004301.

Byerlee, J. D. (1978), Friction of rocks, *Pure Appl. Geophys.*, *116*, 615–626.

Clague, D. A., and G. B. Dalrymple (1988), Age and petrology of alkali postshield and rejuvenated-stage lava from Kauai, Hawaii, *Contrib. Mineral. Petrol.*, *99*, 202–218.

Contreras-Reyes, E., and A. Osses (2010), Lithospheric flexure modeling seaward of the Chile trench: Implications for oceanic plate weakening in the trench outer rise region, *Geophys. J. Int.*, *182*, 97–112.

Contreras-Reyes, E., I. Grevemeyer, A. B. Watts, L. Planert, E. R. Flueh, and C. Peirce (2010), Crustal intrusion beneath the Louisville hotspot track, *Earth Planet. Sci. Lett.*, *289*, 323–333.

Courtney, R. C., and C. Beaumont (1983), Thermally-activated creep and flexture of the oceanic lithosphere, *Nature*, *305*, 201–204.

Davaille, A., and C. Jaupart (1994), Onset of thermal convection in fluids with temperature-dependent viscosity: Application to the oceanic mantle, *J. Geophys. Res.*, *99*, 19,853–19,866.

Davies, G. F. (1988), Ocean bathymetry and mantle convection: 1. Large-scale flow and hotspots, *J. Geophys. Res.*, *93*, 10,467–10,489.

Demouchy, S., A. Tommasi, T. B. Ballaran, and P. Cordier (2013), Low strength of Earth's uppermost mantle inferred from tri-axial deformation experiments on dry olivine crystals, *Phys. Earth Planet. Inter.*, *220*, 37–49.

Detrick, R. S., and G. M. Purdy (1980), The structure of the Kane Fracture Zone from seismic refraction studies, *J. Geophys. Res.*, *85*, 3759–3778.

England, P., and P. Molnar (1997), Active deformation of Asia: From kinematics to dynamics, *Science*, *278*, 647–650.

Evans, B., and C. Goetze (1979), The temperature variation of hardness of olivine and its implication for polycrystalline yield stress, *J. Geophys. Res.*, *84*, 5505–5524.

Foley, B., and T. W. Becker (2009), Generation of plate tectonics and mantle heterogeneity from a spherical, visco-plastic convection model, *Geochem. Geophys. Geosyst.*, *10*, Q08001, doi:10.1029/2009GC002378.

Forsyth, D. W. (1985), Subsurface loading estimates of the flexural rigidity of continental lithosphere, *J. Geophys. Res.*, *90*, 12,623–12,632.

Freed, A. M., T. Herring, and R. Bürgmann (2010), Steady-state laboratory flow laws alone fail to explain post-seismic observations, *Earth Planet. Sci. Lett.*, *300*, 1–10.

Goetze, C., and B. Evans (1979), Stress and temperature in the bending lithosphere as constrained by experimental rock mechanics, *Geophys. J. R. Astron. Soc.*, *59*, 463–478.

Gurnis, M., S. Zhong, and J. Toth (2000), On the competing roles of fault reactivation and brittle failure in generating plate tectonics from mantle convection, in *The History and Dynamics of Global Plate Motions*, Geophys. Monogr. Ser., vol. 121, edited by M. A. Richards, R. Gordon, and R. van der Hilst, pp. 73–94, AGU, Washington, D. C.

Hager, B. H., and M. A. Richards (1989), Long-wavelength variations in Earth's geoid: Physical models and dynamical implications, *Philos. Trans. R. Soc. London, Ser. A*, *328*, 309–327.

Hillier, J. K., and A. B. Watts (2005), Relationship between depth and age in the North Pacific Ocean, *J. Geophys. Res.*, *110*, B02405, doi:10.1029/2004JB003406.

Hirth, G., and D. L. Kohlstedt (1996), Water in the oceanic upper mantle: Implications for rheology, melt extraction and the evolution of the lithosphere, *Earth Planet. Sci. Lett.*, *144*, 93–108.

Hirth, G., and D. L. Kohlstedt (2003), Rheology of the upper mantle and the mantle wedge: A view from the experimentalists, in *Inside the Subduction Factory*, Geophysical Monograph, vol. 138, edited by J. Eiler, pp. 83–105, AGU, Washington, D. C.

Höink, T., A. Lenardic, and M. A. Richards (2012), Depth-dependent viscosity and mantle stress amplification: Implications for the role of the asthenosphere in maintaining plate tectonics, *Geophys. J. Int.*, *191*, 30–41, doi:10.1111/j.1365-246X.2012.05621.x.

van Hunen, J., S. Zhong, N. M. Shapiro, and M. H. Ritzwoller (2005), New evidence for dislocation creep from 3-D geodynamic modeling the Pacific upper mantle structure, *Earth Planet. Sci. Lett.*, *238*, 146–155.

Jaroslow, G. E., G. Hirth, and H. J. B. Dick (1996), Abyssal peridotite mylonites: implications for grain-size sensitive flow and strain localization in the oceanic lithosphere, *Tectonophysics*, *256*, 17–37.

Judge, A. V., and M. K. McNutt (1991), The relationship between plate curvature and elastic plate thickness: A study of the Peru-Chile trench, *J. Geophys. Res.*, *96*(B10), 16,625–16,639.

Kanamori, H. (1980), The state of stress in the Earth's lithosphere, in *Physics of the Earth's Interior*, edited by A. Dziewonski and E. Boschi, pp. 531–554, North Holland Publishing Co., Amsterdam, The Netherlands.

Karato, S.-I. (2008), *Deformation of Earth Materials: An Introduction to the Rheology of Solid Earth*, Cambridge Univ. Press, Cambridge, U. K.

Karato, S.-I., and H. Jung (2003), Effects of pressure on high-temperature dislocation creep in olivine, *Philos. Mag.*, *83*, 401–414.

Karato, S.-I., and P. Wu (1993), Rheology of the upper mantle, *Science*, *260*, 771–778.

Katayama, I., and S.-I. Karato (2008), Low-temperature, high-stress deformation of olivine under water-saturated conditions, *Phys. Earth Planet. Inter.*, *168*, 125–133.

King, S. D. (1995), The viscosity structure of the mantle, in *Reviews of Geophysics (Supplement) U.S. 1991–1994*, pp. 11–17, AGU, Washington, D. C.

Kohlstedt, D. L., and S. J. Mackwell (2009), Strength and deformation of planetary lithospheres, in *Planetary Tectonics*, edited by T. Waters and R. Schultz, pp. 395–455, Cambridge Univ. Press, New York.

Kohlstedt, D. L., B. Evans, and S. J. Mackwell (1995), Strength of the lithosphere: Constraints imposed by laboratory experiments, *J. Geophys. Res.*, *100*, 17,587–17,602.

Lachenbruch, A. H., and J. H. Sass (1988), The stress heat flux paradox and thermal results from Cajon Pass, *Geophys. Res. Lett.*, *15*, 981–984.

Lenardic, A., L. Moresi, and H. Muhlhaus (2003), Longevity and stability of cratonic lithosphere: insights from numerical simulations of coupled mantle convection and continental tectonics, *J. Geophys. Res.*, *108*(B6), 2303, doi:10.1029/2002JB001859.

Ludwig, K. R., B. J. Szabo, J. G. Moore, and K. R. Simmons (1991), Crustal subsidence rate off Hawaii, determined from 234U/238U ages of drowned coral reefs, *Geology*, *19*, 171–174.

Luis, J. F., and M. C. Neves (2006), The isostatic compensation of the Azores Plateau: A 3D admittance and coherence analysis, *J. Volcanol. Geothermal Res.*, *156*, 10–22.

McNutt, M. K. (1980), Implications of regional gravity for state of stress in the Earth's crust and upper mantle, *J. Geophys. Res.*, *85*, 6377–6396.

Mei, S., A. M. Suzuki, D. L. Kohlstedt, N. A. Dixon, and W. B. Durham (2010), Experimental constraints on the strength of the lithospheric mantle, *J. Geophys. Res.*, *115*, B08204, doi:10.1029/2009JB006873.

Milne, G. A., W. R. Gehrels, C. W. Hughes, and M. E. Tamisiea (2009), Identifying the causes of sea- level change, *Nat. Geosci.*, *2*, 471–478.

Mitrovica, J., and A. M. Forte (1997), Radial profile of mantle viscosity: Results from the joint inversion of convection and postglacial rebound observables, *J. Geophys. Res.*, *102*, 2751–2769.

Mitrovica, J. X. (1996), Haskell [1935] revisited, *J. Geophys. Res.*, *101*(B1), 555–570.

Moore, J. G., and D. A. Clague (1992), Volcano growth and evolution of the island of Hawaii, *Geol. Soc. Am. Bull.*, *104*, 1471–1484.

Moore, J. G., and J. F. Campbell (1987), Age of tilted reefs, Hawaii, *J. Geophys. Res.*, *92*, 2641–2646.

Moresi, L., and V. Solomatov (1998), Mantle convection with a brittle lithosphere: Thoughts on the global tectonic styles of the Earth and Venus, *Geophys. J. Int.*, *133*, 669–682.

Morgan, W. J. (1971), Convection plumes in the lower mantle, *Nature*, *230*, 42–43.

Muller, R. D., W. R. Roest, J. Y. Royer, L. M. Gahagan, and J. G. Sclater (1997), Digital isochrones of the world's ocean floor, *J. Geophys. Res.*, *102*, 3211–3214.

Muller, R. D., M. Sdrolias, C. Gaina, and W. R. Roest (2008), Age, spreading rates, and spreading asymmetry of the world's ocean crust, *Geochem. Geophys. Geosyst.*, *9*, Q04006, doi:10.1029/2007GC001743.

Ohuchi, T., S.-I. Karato, and K. Fujino (2010), Strength of single-crystal orthopyroxene under lithospheric conditions, *Contrib. Mineral. Petrol.*, *161*, 961–975.

Olson, P. (1990), Hot spots, swells and mantle plumes, in *Magma Transport and Storage*, edited by M. P. Ryan, pp. 33–51, John Wiley, New York.

Paulson, A., S. J. Zhong, and J. Wahr (2007), Inference of mantle viscosity from GRACE and relative sea level data, *Geophys. J. Int.*, *171*, 497–508.

Peltier, W. R. (1976), Glacial isostatic adjustment: II. The inverse problem, *Geophys. J. R. Astron. Soc.*, *46*, 669–705.

Peltier, W. R. (1998), Implications variations for climate in the level of the sea, *Dyn. Solid Earth*, *98*, 603–689.

Podolefsky, N. S., S. J. Zhong, and A. K. McNamara (2004), The anisotropic and rheological structure of the oceanic upper mantle from a simple model of plate shear, *Geophys. J. Int.*, *158*, 287–296.

Pritchard, M. E., A. M. Rubin, and C. J. Wolfe (2007), Do flexural stresses explain the mantle fault zone beneath Kilauea volcano?, *Geophys. J. Int.*, *168*, 419–430.

Ranero, C., J. Phipps, K. McIntosh, and C. Reichert (2003), Bending-related faulting and mantle serpentinization at the Middle America trench, *Nature*, *425*, 367–373.

Raterron, P., Y. Wu, D. J. Weidner, and J. Chen (2004), Low-temperature olivine rheology at high pressure, *Phys. Earth Planet. Inter.*, *145*, 149–159.

Ribe, N. M., and U. R. Christensen (1994), 3-Dimensional modeling of plume-lithosphere interaction, *J. Geophys. Res.*, *99*, 669–682.

Richards, M. A., W. S. Yang, J. R. Baumgardner, and H.-P. Bunge (2001), Role of a low-viscosity zone in stabilizing plate tectonics: Implications for comparative terrestrial planetology, *Geochem. Geophys. Geosyst.*, *2*, 2000GC000115, doi:10.1029/2000GC000115.

Richards, M. A., E. Contreras-Reyes, C. Lithgow-Bertelloni, M. Ghiorso, and L. Stixrude (2013), Petrological interpretation of deep crustal intrusive bodies beneath oceanic hotspot provinces, *Geochem. Geophys. Geosyst.*, *14*, 604–619, doi:10.1029/2012GC004448.

Ritzwoller, M. H., N. M. Shapiro, and S. J. Zhong (2004), Cooling history of the Pacific lithosphere, *Earth Planet. Sci. Lett.*, *226*, 69–84.

Ruepke, L., K. Iyer, and J. Phipps Morgan (2009), Simulations of oceanic lithosphere serpentinization, *Geophys. Res. Abstr.*, *11*, EGU2009–13,212.

Shor, G. G., and D. D. Pollard (1964), Mohole site selection studies north of Maul, *J. Geophys. Res.*, *69*, 1627–1637.

Stein, C. A., and S. Stein (1992), A model for the global variation in oceanic depth and heat flow with lithospheric age, *Nature*, *359*, 123–129.

Tackley, P. J. (2000), Self-consistent generation of tectonic plates in time-dependent, three-dimensional mantle convection simulations 2. Strain weakening and asthenosphere, *Geochem. Geophys. Geosyst.*, *1*, 2000GC000043, doi:10.1029/2000GC000043.

Tarduno, J. A., et al. (2003), The Emperor Seamounts: Southward motion of the Hawaiian hotspot plume in Earth's mantle, *Science*, *301*, 1064–1069.

Turcotte, D. L., and G. Schubert (2002), *Geodynamics*, 2nd ed., 456 p., Cambridge Univ. Press, New York.

van Heck, H., and P. J. Tackley (2008), Planforms of self-consistently generated plate tectonics in 3-D spherical geometry, *Geophys. Res. Lett.*, *35*, L19312, doi:10.1029/2008GL035190.

von Herzen, R. P., M. J. Cordery, R. S. Detrick, and C. Fang (1989), Heat flow and the thermal origin of hot spot swells: The Hawaiian swell revisited, *J. Geophys. Res.*, *94*, 13,783–13,799.

Warren, J. M., and G. Hirth (2006), Grain size sensitivity deformation mechanisms in naturally deformed peridotites, *Earth Planet. Sci. Lett.*, *248*, 438–450.

Watts, A. B. (1978), An analysis of isostasy in the world's oceans 1. Hawaiian-Emperor seamount chain, *J. Geophys. Res.*, *83*, 5989–6004.

Watts, A. B., J. H. Bodine, and N. M. Ribe (1980), Observations of flexure and the geological evolution of the Pacific Ocean basin, *Nature*, *283*, 532–537.

Watts, A. B. (2001), *Isostasy and Flexure of the Lithosphere*, 472 p., Cambridge Univ. Press, Cambridge.

Watts, A. B., and S. J. Zhong (2000), Observations of flexure and the rheology of oceanic lithosphere, *Geophys. J. Int.*, *142*, 855–875.

Watts, A. B., and U. S. ten Brink (1989), Crustal structure, flexure and subsidence history of the Hawaiian Islands, *J. Geophys. Res.*, *94*, 10,473–410,500.

Watts, A. B., U. S. ten Brink, P. Buhl, and T. M. Brocher (1985), A multichannel seismic study of lithospheric flexure across the Hawaiian-Emperor seamount chain, *Nature*, *315*, 105–111.

Watts, A. B., S. J. Zhong, and J. Hunter (2013), The behavior of the lithosphere on seismic to geologic timescales, *Annu. Rev. Earth Planet. Sci.*, *41*, 443–468, doi:10.1146/annurev-earth-042711-105457.

Wessel, P., and W. F. Haxby (1990), Thermal stresses, differential subsidence, and flexure at oceanic fracture zones, *J. Geophys. Res.*, *95*, 375–391.

Wessel, P. (1993), A reexamination of the flexural deformation beneath the Hawaiian islands, *J. Geophys. Res.*, *98*, 12,177–12,190.

Willett, S. D., D. S. Chapman, and H. J. Neugebauer (1985), A thermo-mechanical model of continental lithosphere, *Nature*, *314*, 520–523.

Wolfe, C. J., P. G. Okubo, G. Ekstrom, M. Nettles, and P. M. Shearer (2004), Characteristics of deep (≥13 km) Hawaiian earthquakes and Hawaiian earthquakes west of 155:55°W, *Geochem. Geophys. Geosyst.*, *5*, Q04006, doi:10.1029/2003GC000618.

Wu, P. (1992), Deformation of an incompressible viscoelastic flat earth with power-law creep: A finite-element approach, *Geophys. J. Int.*, *108*(1), 35–51.

Zhong, S. J. (1997), Dynamics of crustal compensation and its influences on crustal isostasy, *J. Geophys. Res.*, *102*, 15,287–15,299.

Zhong, S. J., and A. B. Watts (2002), Constraints on the dynamics of mantle plumes from uplift of Hawaiian islands, *Earth Planet. Sci. Lett.*, *203*, 105–116.

Zhong, S. J., M. Gurnis, and L. Moresi (1998), The role of faults, nonlinear rheology, and viscosity structure in generating plates from instantaneous mantle flow models, *J. Geophys. Res.*, *103*, 15,255–15,268.

Zhong, S. J., A. Paulson, and J. Wahr (2003), Three-dimensional finite element modeling of Earth's viscoelastic deformation: Effects of lateral variations in lithospheric thickness, *Geophys. J. Int.*, *155*, 679–695.

Zhong, S. J., N. Zhang, Z. X. Li, and J. H. Roberts (2007a), Supercontinent cycles, true polar wander, and very long-wavelength mantle convection, *Earth Planet. Sci. Lett.*, *261*, 551–564.

Zhong, S. J., M. Ritzwoller, N. Shapiro, W. Landuyt, J. Huang, and P. Wessel (2007b), Bathymetry of the Pacific Plate and its implications for thermal evolution of lithosphere and mantle dynamics, *J. Geophys. Res.*, *112*, B06412, doi:10.1029/2006JB004628.

Zoback, M. D., and J. Townend (2001), Implications of hydrostatic pore pressures and high crustal strength for the deformation of intraplate lithosphere, *Tectonophysics*, *336*, 19–30.

Zucca, J. J., D. P. Hill, and R. L. Kovach (1982), Crustal structure of Mauna Loa Volcano, Hawaii, from seismic refraction and gravity data, *Bull. Seismol. Soc. Am.*, *72*, 1535–1550.

Zucca, J. J., and D. P. Hill (1980), Crustal structure of the southeast flank of Kilauea volcano, Hawaii, from seismic refraction measurements, *Bull. Seismol. Soc. Am.*, *70*, 1149–1159.